The Pennsylvania State University
APPLIED RESEARCH LABORATORY
P.O. Box 30
State College, PA 16804

Sensorless Electric Drive for Permanent Magnet Synchronous Motors

by

Todd D. Batzel
Research Assistant

Technical Report No. TR 99-006
October 1999

19991110 128

REPORT DOCUMENTATION PAGE

Form Approved
OMB No. 0704-0188

1. REPORT DATE (DD-MM-YYYY)	2. REPORT DATEX Type	3. DATES COVERED (From - To)
18 October 1999	Final Report	June 1998 to August 1999

4. TITLE AND SUBTITLE

Sensorless Electric Drive for Permanent Magnet Synchromous Motors

5a. CONTRACT NUMBER

5b. GRANT NUMBER
N00014-98-1-0718

5c. PROGRAM ELEMENT NUMBER

6. AUTHOR(S)

Batzel, Todd D.

5d. PROJECT NUMBER
1750

5e. TASK NUMBER

5f. WORK UNIT NUMBER

7. PERFORMING ORGANIZATION NAME(S) AND ADDRESS(ES)

Applied Research Laboratory
P.O. Box 30
State College, PA 16804

8. PERFORMING ORGANIZATION REPORT NUMBER

TR 99-006

9. SPONSORING/MONITORING AGENCY NAME(S) AND ADDRESS(ES)

Naval Undersea Warfare Center

10. SPONSOR/MONITOR'S ACRONYM(S)

NUWC

11. SPONSORING/MONITORING AGENCY REPORT NUMBER

12. DISTRIBUTION AVAILABILITY STATEMENT

Approved for public release.

13. SUPPLEMENTARY NOTES

14. ABSTRACT
The development and availability of very high energy permanent magnet materials has contributed to an increased use of the permanent magnet synchronous motor (PMSM) in high performance underwater applications. The PMSM offers advantages such as increased efficiency, superior torque-to-volume and power-to-volume ratios, and quiet operation. These advantages have resulted in the Navy considering a switch from its present induction motor technology to the PMSM. In order to individually control stator current and angle and thus fully exploit the characteristics of the PMSM, high resolution rotor angle information is required. An encoder or resolver attached to the shaft of the motor normally provides this rotor position information. Such devices add length, size, and inertia to the machine, raise system cost, and present reliability issues in harsh underwater environments. The drawbacks of the rotor position sensor have led to an intense interest in rotor position *sensorless* operation of the PMSM. This study develops a sensorless electric drive strategy suitable to the PMSM. The proposed sensorless strategy is implemented in hardware and tested on several permanent magnet machine types. The implementation of the sensorless drive is discussed, and the performance of the developed system is evaluated. Experimental results show that the rotor position estimation strategy performs well under various steady state and transient conditions.

15. SUBJECT TERMS

Sensorless, Electric Drive, Permanent Magnet Synchronous Motor

16. SECURITY CLASSIFICATION OF:			17. LIMITATION OF ABSTRACT	18. NUMBER OF PAGES	19a. NAME OF RESPONSIBLE PERSON
a. REPORT	b. ABSTRACT	c. THIS PAGE			Todd D. Batzel
U	U	U			19b. TELEPONE NUMBER (Include area code) 814-863-7338

Standard Form 298 (Rev. 8-98)
Prescribed by ANSI-Std Z39-18

Abstract

The development and availability of very high energy permanent magnet materials has contributed to an increased use of the permanent magnet synchronous motor (PMSM) in high performance underwater applications. The PMSM offers advantages such as increased efficiency, superior torque-to-volume and power-to-volume ratios, and quiet operation. These advantages have resulted in the Navy considering a switch from its present induction motor technology to the PMSM. In order to individually control stator current and angle and thus fully exploit the characteristics of the PMSM, high resolution rotor angle information is required. An encoder or resolver attached to the shaft of the motor normally provides this rotor position information. Such devices add length, size, and inertia to the machine, raise system cost, and present reliability issues in harsh underwater environments. The drawbacks of the rotor position sensor have led to an intense interest in rotor position *sensorless* operation of the PMSM. This study develops a sensorless electric drive strategy suitable to the PMSM. The proposed sensorless strategy is implemented in hardware and tested on several permanent magnet machine types. The implementation of the sensorless drive is discussed, and the performance of the developed system is evaluated. Experimental results show that the rotor position estimation strategy performs well under various steady state and transient conditions.

Table of Contents

List of Figures

List of Tables

List of Symbols

Abbreviation	Variable	Unit
λ	flux linkage	Wb=V-s
ω	angular frequency	rad/s
θ	angle	rad
$s = \sigma + j\omega$	LaPlace Variable	rad/s
R	resistance	ohm
L	inductance	H
T	torque	n-m
J	inertia	kg-m^2
i	current	A
v	voltage	V
e	induced voltage (emf)	V
P	number of Poles	none
$\mathcal{L}$	LaPlace operator	
$\mathcal{L}^{1}$	Inverse LaPlace operator	

1 INTRODUCTION

The United States Navy is actively pursuing electric drive systems for future Navy vessels including submarines, aircraft carriers, and surface combatants. Electric drive systems for propulsion can eliminate the need for propeller shafts and gearing. In addition, it increases vehicle stealth and flexibility.

The Navy has invested significant time and money into its present induction motor technology, which is larger and noisier than permanent magnet motor technology. Even more investment is planned over the next several years to develop a new electric drive technology to power new vehicles. Given the advantages of the permanent magnet synchronous motor (PMSM), it is likely that this new electric drive development will include a switch to a permanent magnet system. The advantages of the PMSM over the induction motor technology include increased power density, efficiency, and acoustic performance. Another advantage to permanent magnet technology over the Navy's IPS (induction) technology is a motor technology that can be used interchangeably between surface combatants and submarines, and eventually aircraft carriers.

In order to fully exploit the characteristics of the PMSM, high resolution rotor angle information is required. A resolver or encoder attached to the shaft of the machine usually provides this information. Many Navy applications, however, cannot tolerate the use of the position sensor because of space and weight limitations, reliability concerns, or packaging issues. Thus, there has been an intense interest in the development of a so-called *position sensorless* drive, where the PMSM stator itself is used as the rotor position sensor.

1.1 Statement of Problem

Along with the recent interest in the PMSM by both military and industry came the development of new and innovative inverter topologies [1, 2, 3]. Also, many new control techniques for current and direct torque control [4, 5], efficiency maximization [6], and torque ripple minimization [7, 8, 9] of the PMSM have been presented. Each of these control techniques requires accurate knowledge of the rotor angle in order to be effective. Typically, a resolver or encoder attached to the shaft of the rotor provides the required rotor angle information. These devices add size, length, and inertia to the motor and present serious reliability issues to many applications such as a harsh underwater environment or a submerged propulsion motor for undersea vehicles.

The requirement for high resolution rotor position information coupled with the unreliability of the rotor position transducers in an underwater environment has created a need for a rotor position *sensorless* strategy suitable for such Navy applications. The extremely compact package achievable with a sensorless PMSM results in additional payload volume that can be used to increase energy storage, mission capabilities, and

1

endurance. Elimination of the high resolution rotor position sensors enhances the value of using the PMSM in Navy applications.

1.2   Statement of Purpose

In this document, the development and implementation of a sensorless PMSM drive is presented. The design and the theory of operation of the sensorless drive is discussed. Implementation issues are addressed, and experimental results are used to show the validity of the design techniques. Through experimentation, the developed sensorless strategy will be shown to result in Naval electric drive capabilities that fully utilize many of the attractive characteristics of the PMSM without the requirement for a high resolution position sensor.

1.3   Organization of Report

This document focuses on the design and implementation of a rotor position estimator for the PMSM. In Chapter 2, a detailed model of the PMSM is developed in several frames of reference. The models are used to perform the design and to support simulations of the sensorless PMSM drive. The developed PMSM equations serve as the reference model in the rotor position observer presented in Chapter 3.

The PMSM model is, through some mild assumptions, manipulated into a linear form in Chapter 3. This allows the use of well-established linear control systems tools to be applied to the system. Using the linearized model, a Luenberger observer is designed to perform the rotor position estimation task.

The observer design presented in Ch. 3 is followed up with an implementation of the sensorless drive in hardware. The implementation of the sensorless drive and associated issues with its performance is discussed in Ch. 4. The performance of the resulting sensorless drive is verified through extensive real-time experiments, and results are discussed.

2 PMSM MODEL

In this section, the arithmetic model for a permanent magnet synchronous motor is presented. The models developed in this section serve as the basis for the design of sensorless PMSM drive in the subsequent chapters. The PMSM equations are developed in both the stationary and rotating reference frames. Assumptions in developing the mathematical model are:

- Saturation is neglected
- Motor back EMF is sinusoidal
- Eddy currents and hysteresis effects are neglected
- Balanced three phase supply and currents are assumed
- Air gap reluctance has a constant and sinusoidally varying (with position) component
- Inductance, resistance and back emfs are symmetrical

2.1 Machine Equations

Fig. 1 shows a two-pole, three-phase surface mounted PMSM, where the stator windings (phase a, b, and c) are identical sinusoidally distributed windings. In this section, the flux linkage and voltage equations for this machine are established in the stationary reference frame. Two coordinate transformations (sometime referred to as the Clarke and Park transformations) are then applied to obtain the machine equations in the two-phase stationary and rotor reference frames, respectively. A state space model of the machine results from these differential equations.
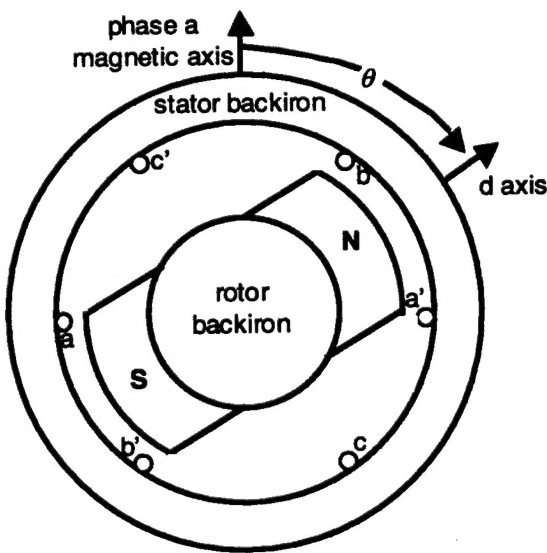
Fig. 1 Analytical model of PMSM in stationary reference frame

2.1.1 Stationary Reference Frame Equations

In the stationary reference frame the machine variables are associated with circuits that are stationary, or fixed to the stator. Thus, the dynamic equations are derived from the three-phase model of the motor shown in Fig. 1. The flux linking the three phases of the PMSM in the stationary reference frame may be represented by

$$
\begin{bmatrix} \lambda_a \\ \lambda_b \\ \lambda_c \end{bmatrix} = \begin{bmatrix} L_{aa}(\theta) & L_{ab}(\theta) & L_{ca}(\theta) \\ L_{ab}(\theta) & L_{bb}(\theta) & L_{bc}(\theta) \\ L_{ca}(\theta) & L_{bc}(\theta) & L_{cc}(\theta) \end{bmatrix} \begin{bmatrix} i_a \\ i_b \\ i_c \end{bmatrix} + \begin{bmatrix} \lambda_m \cos(\theta) \\ \lambda_m \cos\left(\theta - \frac{2\pi}{3}\right) \\ \lambda_m \cos\left(\theta + \frac{2\pi}{3}\right) \end{bmatrix}, \tag{1}
$$

where L_{aa}, L_{bb}, and L_{cc} are the self inductances of windings a, b, and c respectively. Similarly, L_{ab}, L_{bc}, and L_{ca} represent the mutual inductance terms between windings ab, bc, and ca respectively. The flux linkage produced by the rotating permanent magnet is represented by λ_m. Although the self and mutual inductances of a non-salient rotor machine are in general not dependent on the rotor position θ, the terms in (1) are written as a function of the rotor angle for application to salient rotor machines as well.

The self inductances shown in (1) may now be written as

$$
\begin{aligned}
L_{aa}(\theta) &= L_l + L_{av} - L_\theta \cos(2\theta) \\
L_{bb}(\theta) &= L_l + L_{av} - L_\theta \cos\left(2\theta + \frac{2\pi}{3}\right) \\
L_{cc}(\theta) &= L_l + L_{av} - L_\theta \cos\left(2\theta - \frac{2\pi}{3}\right)
\end{aligned} \tag{2}
$$

where L_l, L_{av}, and L_θ are the leakage, average and position dependent inductances, respectively. In the case of a non-salient machine, L_θ approaches a value of zero. The mutual inductance terms are represented by

$$
\begin{aligned}
L_{ab}(\theta) &= -\frac{L_{av}}{2} - L_\theta \cos\left(2\theta - \frac{2\pi}{3}\right) \\
L_{bc}(\theta) &= -\frac{L_{av}}{2} - L_\theta \cos(2\theta) \\
L_{ca}(\theta) &= -\frac{L_{av}}{2} - L_\theta \cos\left(2\theta + \frac{2\pi}{3}\right)
\end{aligned} \tag{3}
$$

The voltage equation in the stationary frame may be written as

$$
\begin{bmatrix} v_a \\ v_b \\ v_c \end{bmatrix} = \begin{bmatrix} R & 0 & 0 \\ 0 & R & 0 \\ 0 & 0 & R \end{bmatrix} \begin{bmatrix} i_a \\ i_b \\ i_c \end{bmatrix} + \frac{d}{dt} \begin{bmatrix} \lambda_a \\ \lambda_b \\ \lambda_c \end{bmatrix},
\tag{4}
$$

where v_a, v_b, and v_c are the line-to-neutral or phase voltages of windings a, b, and c, and R is the per phase resistance of the stator. Next, substituting the flux linkage expressions of (1-3) into (4) and taking the derivative yields

$$
\begin{bmatrix} v_a \\ v_b \\ v_c \end{bmatrix} = \begin{bmatrix} R & 0 & 0 \\ 0 & R & 0 \\ 0 & 0 & R \end{bmatrix} \begin{bmatrix} i_a \\ i_b \\ i_c \end{bmatrix} + \mathbf{L}_3 \begin{bmatrix} \dot{i}_a \\ \dot{i}_b \\ \dot{i}_c \end{bmatrix} + \omega_e \mathbf{L}_3' \begin{bmatrix} i_a \\ i_b \\ i_c \end{bmatrix} - \omega_e \lambda_m \begin{bmatrix} \sin(\theta) \\ \sin\left(\theta - \tfrac{2\pi}{3}\right) \\ \sin\left(\theta + \tfrac{2\pi}{3}\right) \end{bmatrix},
\tag{5}
$$

where the dot ($\dot{\ }$) placed directly over a variable indicates the time derivative operator, the inductance matrix in three-phase stationary coordinates is

$$
\mathbf{L}_3 = \begin{bmatrix}
L_l + L_{av} - L_\theta \cos(2\theta) & -\dfrac{L_{av}}{2} - L_\theta \cos\left(2\theta - \dfrac{2\pi}{3}\right) & -\dfrac{L_{av}}{2} - L_\theta \cos\left(2\theta + \dfrac{2\pi}{3}\right) \\[3mm]
-\dfrac{L_{av}}{2} - L_\theta \cos\left(2\theta - \dfrac{2\pi}{3}\right) & L_l + L_{av} - L_\theta \cos\left(2\theta + \dfrac{2\pi}{3}\right) & -\dfrac{L_{av}}{2} - L_\theta \cos(2\theta) \\[3mm]
-\dfrac{L_{av}}{2} - L_\theta \cos\left(2\theta + \dfrac{2\pi}{3}\right) & -\dfrac{L_{av}}{2} - L_\theta \cos(2\theta) & L_l + L_{av} - L_\theta \cos\left(2\theta - \dfrac{2\pi}{3}\right)
\end{bmatrix}
\tag{6}
$$

and its derivative with respect to the rotor angle is

$$
\mathbf{L}_3' = \begin{bmatrix}
2L_\theta \sin(2\theta) & 2L_\theta \sin\left(2\theta - \dfrac{2\pi}{3}\right) & 2L_\theta \sin\left(2\theta + \dfrac{2\pi}{3}\right) \\[3mm]
2L_\theta \sin\left(2\theta - \dfrac{2\pi}{3}\right) & 2L_\theta \sin\left(2\theta + \dfrac{2\pi}{3}\right) & 2L_\theta \sin(2\theta) \\[3mm]
2L_\theta \sin\left(2\theta + \dfrac{2\pi}{3}\right) & 2L_\theta \sin(2\theta) & 2L_\theta \sin\left(2\theta - \dfrac{2\pi}{3}\right)
\end{bmatrix}.
\tag{7}
$$

An expression for the torque generated by the PMSM may be obtained by using the coenergy of the electromagnetic system [10]. The coenergy is defined as

$$
\begin{aligned}
W_c(i_a, i_b, i_c, \theta) = &\int_0^{i_{c0}} \lambda_c (i_a = 0, i_b = 0, i_c, \theta) di_c + \int_0^{i_{b0}} \lambda_b (i_a = 0, i_b, i_{c0}, \theta) di_b \\
&+ \int_0^{i_{a0}} \lambda_a (i_a, i_{b0}, i_{c0}, \theta) di_a
\end{aligned}
\tag{8}
$$

and the torque may be determined from the coenergy by

$$T(i_a, i_b, i_c, \theta) = \frac{\partial W_c}{\partial \theta_{mech.}} = \frac{P}{2} \frac{\partial W_c}{\partial \theta} \quad , \tag{9}$$

where P is the number of PMSM poles. By substituting (1) into the coenergy expression, the coenergy for the PMSM in the stationary reference frame is found to be

$$W_c = \frac{1}{2} \left(L_{aa} i_a^2 + L_{bb} i_b^2 + L_{cc} i_c^2 \right) + \left(L_{ab} i_a i_b + L_{ca} i_c i_a + L_{bc} i_b i_c \right)$$
$$+ \lambda_m \left(\cos(\theta) i_a + \cos\left(\theta - \frac{2\pi}{3} \right) i_b + \cos\left(\theta + \frac{2\pi}{3} \right) i_c \right) \tag{10}$$

Thus, the torque for the PMSM is

$$T = \frac{P}{2} \left\{ \begin{bmatrix} i_a & i_b & i_c \end{bmatrix} [L_3'] \begin{bmatrix} i_a \\ i_b \\ i_c \end{bmatrix} - \lambda_m \left[\sin(\theta) \quad \sin\left(\theta - \frac{2\pi}{3} \right) \quad \sin\left(\theta + \frac{2\pi}{3} \right) \right] \begin{bmatrix} i_a \\ i_b \\ i_c \end{bmatrix} \right\}, \tag{11}$$

where L_3' is defined by (7).

2.1.2 Two-Phase Stationary Reference Frame Equations

In the two-phase stationary reference frame, the three-phase machine of Fig. 1 is transformed to a machine with two fictitious windings windings α and β, as shown in Fig. 2. In the two-phase stationary reference frame, the voltages, currents, and fluxes are related to the actual physical quantities by a simple linear transformation. The two-phase equivalent model is sometimes preferred to the three-phase model of eq. (5) because it reduces the order of the system equations. This is done without loss of generality to the three-phase system, since the system is assumed to be balanced and symmetric.

The change in variables which transforms three phase variables of stationary circuit elements into a two-phase stationary reference frame has been developed by Clarke [11]. The Clarke transform for the model shown in Fig. 2 is written as

$$f_{\alpha,\beta,0} = C f_{a,b,c} ; f_{a,b,c} = C^{-1} f_{\alpha,\beta,0} \quad , \tag{12}$$

where the Clarke transform C is defined as

$$C = \sqrt{\frac{2}{3}} \begin{bmatrix} 1 & -\dfrac{1}{2} & -\dfrac{1}{2} \\ 0 & \dfrac{\sqrt{3}}{2} & -\dfrac{\sqrt{3}}{2} \\ \sqrt{\dfrac{1}{2}} & \sqrt{\dfrac{1}{2}} & \sqrt{\dfrac{1}{2}} \end{bmatrix} , \qquad (13)$$

and

$$C^{-1} = C^T . \qquad (14)$$
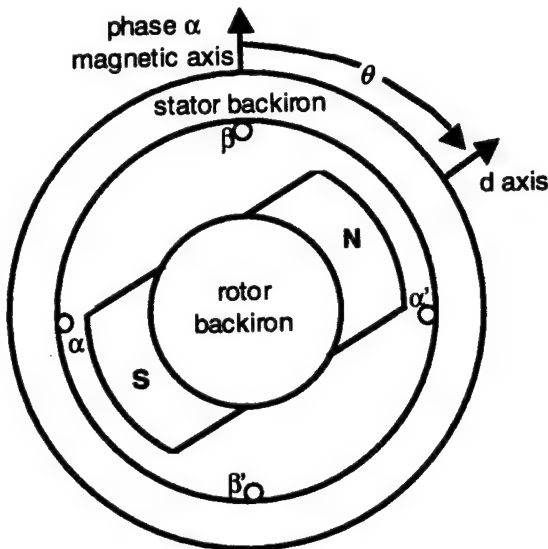
Fig. 2. Analytical Model in the two-phase stationary reference frame

The Clarke transformation in this case is to a subspace in which the zero sequences (f_0) are unreachable. This property is physically imposed by the linear dependence of the stator currents (star connection of windings with inaccessible neutral). The direction of f_α and f_β can be considered to be the direction of the magnetic axes of the new windings created by the change of variables.

Applying the Clarke transformation to the three phase model (5), and assuming no zero-sequence component yields

$$\begin{bmatrix} v_\alpha \\ v_\beta \end{bmatrix} = [\mathbf{L}] \frac{d}{dt} \begin{bmatrix} i_\alpha \\ i_\beta \end{bmatrix} + [\mathbf{R} + \mathbf{L}'] \begin{bmatrix} i_\alpha \\ i_\beta \end{bmatrix} + \sqrt{\frac{3}{2}} \omega_e \lambda_m \begin{bmatrix} -\sin(\theta) \\ \cos(\theta) \end{bmatrix} , \qquad (15)$$

where

$$\mathbf{L} = \begin{bmatrix} L_l + \dfrac{3}{2}L_{av} - \dfrac{3}{2}L_\theta\cos(2\theta) & -\dfrac{3}{2}L_\theta\sin(2\theta) \\[2mm] -\dfrac{3}{2}L_\theta\sin(2\theta) & L_l + \dfrac{3}{2}L_{av} + \dfrac{3}{2}L_\theta\cos(2\theta) \end{bmatrix} \tag{16}$$

and

$$\mathbf{R} + \mathbf{L}' = \begin{bmatrix} R + 3\omega_e L_\theta\sin(2\theta) & -3\omega_e L_\theta\cos(2\theta) \\[2mm] -3\omega_e L_\theta\cos(2\theta) & R - 3\omega_e L_\theta\sin(2\theta) \end{bmatrix}. \tag{17}$$

This may be manipulated into the state space representation

$$\begin{bmatrix} \dot{i}_\alpha \\[2mm] \dot{i}_\beta \end{bmatrix} = \mathbf{L}^{-1}\left\{ \begin{bmatrix} v_\alpha \\ v_\beta \end{bmatrix} - [\mathbf{R}+\mathbf{L}']\begin{bmatrix} i_\alpha \\ i_\beta \end{bmatrix} - \sqrt{\frac{3}{2}}\omega_e\lambda_m\begin{bmatrix} -\sin(\theta) \\ \cos(\theta) \end{bmatrix} \right\}, \tag{18}$$

where

$$\mathbf{L}^{-1} = \frac{1}{L_l^2 + 3L_l L_{av} + \dfrac{9}{4}\left(L_{av}^2 - L_\theta^2\right)} \begin{bmatrix} L_l + \dfrac{3}{2}\left(L_{av} + L_\theta\cos(2\theta)\right) & \dfrac{3}{2}L_\theta\sin(2\theta) \\[2mm] \dfrac{3}{2}L_\theta\sin(2\theta) & L_l + \dfrac{3}{2}\left(L_{av} - L_\theta\cos(2\theta)\right) \end{bmatrix}. \tag{19}$$

An alternate representation in terms of the flux linkages is sometimes useful. This expression is obtained by applying the Clarke Transform to (4), which gives

$$\begin{bmatrix} \dot{\lambda}_\alpha \\[2mm] \dot{\lambda}_\beta \end{bmatrix} = \begin{bmatrix} v_\alpha \\ v_\beta \end{bmatrix} - \begin{bmatrix} R & 0 \\ 0 & R \end{bmatrix}\begin{bmatrix} i_\alpha \\ i_\beta \end{bmatrix}. \tag{20}$$

Applying the Clarke transformation to (1) and solving for the current vector $i_{\alpha\beta}$ gives

$$\begin{bmatrix} i_\alpha \\[2mm] i_\beta \end{bmatrix} = \mathbf{L}^{-1}\left\{ \begin{bmatrix} \lambda_\alpha \\ \lambda_\beta \end{bmatrix} - \sqrt{\frac{3}{2}}\lambda_m\begin{bmatrix} \cos(\theta) \\ \sin(\theta) \end{bmatrix} \right\}. \tag{21}$$

Substituting (21) into (20) yields the differential equations with the flux linkages as the state variables:

$$\begin{bmatrix} \dot{\lambda}_\alpha \\[2mm] \dot{\lambda}_\beta \end{bmatrix} = \begin{bmatrix} v_\alpha \\ v_\beta \end{bmatrix} - R\mathbf{L}^{-1}\left\{ \begin{bmatrix} \lambda_\alpha \\ \lambda_\beta \end{bmatrix} - \sqrt{\frac{3}{2}}\lambda_m\begin{bmatrix} \cos\theta \\ \sin\theta \end{bmatrix} \right\}. \tag{22}$$

The torque expression for two-phase stationary reference frame variables is now derived from the application of the Clarke transform to (1):

$$\begin{bmatrix} \lambda_\alpha \\ \lambda_\beta \end{bmatrix} = [\mathbf{L}]\begin{bmatrix} i_\alpha \\ i_\beta \end{bmatrix} + \sqrt{\frac{3}{2}}\lambda_m \begin{bmatrix} \cos\theta \\ \sin\theta \end{bmatrix} \quad , \tag{23}$$

Similar to the torque expression development in the three-phase reference frame, the coenergy method is used, where the coenergy is now given by

$$W_c = \int_0^{i_{\beta 0}} \lambda_\beta(i_\alpha = 0, i_\beta, \theta)di_\beta + \int_0^{i_{\alpha 0}} \lambda_\alpha(i_\alpha, i_\beta = i_{\beta 0}, \theta)di_\alpha \quad . \tag{24}$$

Performing the operations indicated by (24) yields

$$\begin{aligned} W_c = &\left(L_l + \frac{3}{2}L_{av} + \frac{3}{2}L_\theta \cos(2\theta)\right)\frac{i_\beta^2}{2} + \sqrt{\frac{3}{2}}\lambda_m \sin(\theta)i_\beta \\ &+ \left(L_l + \frac{3}{2}L_{av} - \frac{3}{2}L_\theta \cos(2\theta)\right)\frac{i_\alpha^2}{2} + \left(\left(-\frac{3}{2}L_\theta \sin(2\theta)\right)i_\alpha i_\beta\right) + \sqrt{\frac{3}{2}}\lambda_m \cos(\theta)i_\alpha \end{aligned} \tag{25}$$

Finally, the torque expression is found by applying

$$T(i_\alpha, i_\beta, \theta) = \frac{\partial W_c}{\partial \theta_{mech.}} = \frac{P}{2}\frac{\partial W_c}{\partial \theta} \quad , \tag{26}$$

which results in

$$T = \frac{P}{2}\left(\begin{bmatrix} i_\alpha & i_\beta \end{bmatrix}\begin{bmatrix} \frac{3}{2}L_\theta \sin(2\theta) & -\frac{3}{2}L_\theta \cos(2\theta) \\ -\frac{3}{2}L_\theta \cos(2\theta) & -\frac{3}{2}L_\theta \sin(2\theta) \end{bmatrix}\begin{bmatrix} i_\alpha \\ i_\beta \end{bmatrix} + \sqrt{\frac{3}{2}}\lambda_m\begin{bmatrix} -\sin(\theta) & \cos(\theta) \end{bmatrix}\begin{bmatrix} i_\alpha \\ i_\beta \end{bmatrix}\right). \tag{27}$$

2.1.3 Rotating Reference Frame Equations

In the rotating reference frame, stator variables are transformed to a reference frame that is fixed to the rotor, and therefore rotating at an angular speed ω_e. The Park transformation may be applied to convert from stationary variables to the rotating reference frame (d-q model). The transformation from the two-phase (stationary) model shown in Fig. 2 to a reference frame which is synchronous with the rotor may be written as

$$f_{d,q,0} = P f_{\alpha,\beta,0} \tag{28}$$

where the Park matrix P transforms the two-phase stationary frame variables into the rotating reference frame. The Park matrix is defined as

$$P = \begin{bmatrix} \cos(\theta) & \sin(\theta) & 0 \\ -\sin(\theta) & \cos(\theta) & 0 \\ 0 & 0 & 1 \end{bmatrix}. \tag{29}$$
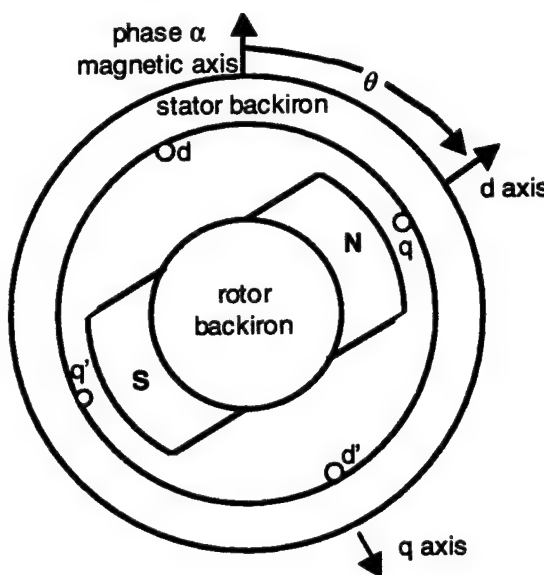
Fig. 3 Analytical model of PMSM in rotating reference frame

Converting three-phase stationary reference frame variables directly to the rotating frame involves the application of both Park and Clarke transforms:

$$f_{d,q,0} = PC f_{a,b,c} = K f_{a,b,c} \; , \tag{30}$$

where

$$K = PC = \sqrt{\frac{2}{3}} \begin{bmatrix} \cos\theta & \cos\left(\theta - \frac{2\pi}{3}\right) & \cos\left(\theta + \frac{2\pi}{3}\right) \\ -\sin\theta & -\sin\left(\theta - \frac{2\pi}{3}\right) & -\sin\left(\theta + \frac{2\pi}{3}\right) \\ \sqrt{\frac{1}{2}} & \sqrt{\frac{1}{2}} & \sqrt{\frac{1}{2}} \end{bmatrix}. \tag{31}$$

Transformations from rotating reference frame to the stationary are performed with (30) and the inverse Park-Clarke matrix:

$$K^{-1} = \sqrt{\frac{2}{3}} \begin{bmatrix} \cos\theta & -\sin\theta & \sqrt{\frac{1}{2}} \\ \cos\left(\theta - \frac{2\pi}{3}\right) & -\sin\left(\theta - \frac{2\pi}{3}\right) & \sqrt{\frac{1}{2}} \\ \cos\left(\theta + \frac{2\pi}{3}\right) & -\sin\left(\theta + \frac{2\pi}{3}\right) & \sqrt{\frac{1}{2}} \end{bmatrix} . \tag{32}$$

To obtain a voltage equation in the rotating reference frame, the Park-Clarke transformations are applied to the voltage equation in the three-phase stationary reference frame (5). After some trigonometric manipulations, the state space form of the PMSM in the rotating reference frame is revealed:

$$\begin{bmatrix} \dot{i}_d \\ \dot{i}_q \\ \dot{i}_0 \end{bmatrix} = \begin{bmatrix} L_d & 0 & 0 \\ 0 & L_q & 0 \\ 0 & 0 & L_l \end{bmatrix}^{-1} \left\{ \begin{bmatrix} v_d \\ v_q \\ v_0 \end{bmatrix} - \begin{bmatrix} R & -\omega_e L_q & 0 \\ \omega_e L_d & R & 0 \\ 0 & 0 & R \end{bmatrix} \begin{bmatrix} i_d \\ i_q \\ i_0 \end{bmatrix} - \sqrt{\frac{3}{2}}\lambda_m \omega_e \begin{bmatrix} 0 \\ 1 \\ 0 \end{bmatrix} \right\} , \tag{33}$$

where the d and q inductances are defined by

$$L_d = \frac{3}{2}L_{av} - \frac{3}{2}L_\theta + L_l \tag{34}$$

and

$$L_q = \frac{3}{2}L_{av} + \frac{3}{2}L_\theta + L_l . \tag{35}$$

A torque expression in rotating coordinates is obtained by applying the Park transformation P to (27). This results in

$$T = \frac{P}{2}\left\{ \underbrace{\begin{bmatrix} i_d & i_q \end{bmatrix} \begin{bmatrix} 0 & -\frac{3}{2}L_\theta \\ -\frac{3}{2}L_\theta & 0 \end{bmatrix} \begin{bmatrix} i_d \\ i_q \end{bmatrix}}_{\text{reluctance torque term}} + \underbrace{\sqrt{\frac{3}{2}}\lambda_m \begin{bmatrix} 0 & 1 \end{bmatrix} \begin{bmatrix} i_d \\ i_q \end{bmatrix}}_{\text{alignment torque term}} \right\} . \tag{36}$$

The first term of (36) represents the reluctance torque, and the second term is the alignment torque. For non-salient machines where L_θ is zero, no reluctance torque is present, and the direct axis current i_d is normally maintained at zero. For machines with buried or inset permanent magnets on the rotor, the reluctance torque term will contribute positively to the total torque when the direct axis current i_d is negative. Thus, in the salient rotor machine, an increase in torque is possible due to the reluctance term. The

11

torque representation in rotating coordinates is often used because it eliminates the angle dependent term that is present in stationary coordinates (11 and 27).

2.2 PMSM Models

2.2.1 Model of Mechanical System

For a rotational system such as the PMSM, the rotational equivalent of Newtons law holds. Thus, the angular acceleration is given by

$$\dot{\omega}_m = \frac{T - T_{load} - B\omega_m}{J_m},$$ (37)

where the torque T generated by the motor is given by (11),(27), or (36), depending on the reference frame of choice. The load torque is represented by T_{load}, viscous friction is B, mechanical speed of the rotor is ω_m, and rotational inertia of the system is J_m. The mechanical rotor angle θ_m derivative gives the rotor mechanical speed:

$$\dot{\theta}_m = \omega_m.$$ (38)

The number of poles P relates the mechanical variables (with m subscript) to their electrical counterparts as stated in the following:

$$\omega_e = \frac{P}{2}\omega_m$$ (39)

$$\theta = \frac{P}{2}\theta_m.$$ (40)

2.2.2 Electromechanical Model in the Three-phase Stationary Reference Frame

In this section, the electrical equations of the PMSM in the three-phase stationary reference frame are combined with the mechanical equations developed in the previous section to form a complete PMSM model that is suitable for simulations of the PMSM. Although the rotating reference frame model is often used to model the PMSM, this model makes it difficult to incorporate system asymmetries, faults, and the effects of the associated electronics. Thus, the stationary reference frame will be used so that imperfections such as offsets, flux harmonics, and pulse width modulation effects may easily be accounted for, if necessary.

The phase voltage equations in the three-phase stationary reference frame given in (5-7) can be modified to reflect the line-to-line voltages. This eliminates the need for

calculating the phase voltages, which can be difficult due to the buried neutral connection. For such a connection, there may be no zero-sequence current so that

$$i_a + i_b + i_c = 0 . \tag{41}$$

Using (41), the line voltages are obtained from (5):

$$v_{ab} = i_a \left(R + \omega_e L_{11}' - \omega_e L_{21}' - \omega_e L_{13}' + \omega_e L_{23}'\right) + i_b \left(\omega_e L_{12}' - R - \omega_e L_{22}' - \omega_e L_{13}' + \omega_e L_{23}'\right)$$
$$+ \frac{di_a}{dt}\left(L_{11} - L_{21} - L_{13} + L_{23}\right) + \frac{di_b}{dt}\left(L_{12} - L_{22} - L_{13} + L_{23}\right) + \sqrt{3}\omega_e \lambda_n \sin\left(\theta - \left(5\pi/6\right)\right) \tag{42}$$

$$v_{bc} = i_a \left(R + \omega_e L_{21}' - \omega_e L_{31}' - \omega_e L_{23}' + \omega_e L_{33}'\right) + i_b \left(\omega_e L_{22}' + 2R - \omega_e L_{32}' - \omega_e L_{23}' + \omega_e L_{33}'\right)$$
$$+ \frac{di_a}{dt}\left(L_{21} - L_{31} - L_{23} + L_{33}\right) + \frac{di_b}{dt}\left(L_{22} - L_{32} - L_{23} + L_{33}\right) + \sqrt{3}\omega_e \lambda_n \sin\left(\theta - \left(\pi/2\right)\right) \tag{43}$$

where the inductances L_{xy} and L_{xy}' correspond to the row x, column y entry in the three-phase reference frame inductance matrices defined in (6) and (7) respectively. Inserting these inductance entries from (6) and (7) into (42) and (43) and then simplifying yields:

$$v_{ab} = i_a \left(R + 6\omega_e L_\theta \sin(2\theta)\right) + i_b \left(-6\omega_e L_\theta \sin\left(2\theta + \frac{2\pi}{3}\right) - R\right)$$
$$+ \frac{di_a}{dt}\left(L_l + \frac{3}{2}L_{av} - 3L_\theta \cos(2\theta)\right) + \frac{di_b}{dt}\left(-L_l - \frac{3}{2}L_{av} + 3L_\theta \cos\left(2\theta + \frac{2\pi}{3}\right)\right) \tag{44}$$
$$+ \sqrt{3}\omega_e \lambda_n \sin\left(\theta - \frac{5\pi}{3}\right)$$

and

$$v_{bc} = i_a \left(R + 6\omega_e L_\theta \sin\left(2\theta - \frac{2\pi}{3}\right)\right) + i_b \left(2R - 6\omega_e L_\theta \sin(2\theta)\right)$$
$$+ \frac{di_a}{dt}\left(L_l + \frac{3}{2}L_{av} - 3L_\theta \cos\left(2\theta - \frac{2\pi}{3}\right)\right) + \frac{di_b}{dt}\left(2L_l + 3L_{av} + 3L_\theta \cos(2\theta)\right) . \tag{45}$$
$$+ \sqrt{3}\omega_e \lambda_n \sin\left(\theta + \frac{\pi}{2}\right)$$

The above line-to-line voltage equations can be put into the matrix representation:

$$\begin{Bmatrix} \begin{bmatrix} \dot{i}_a \\ \dot{i}_b \end{bmatrix} = \begin{bmatrix} \dfrac{2L_l + 3L_{av} + 3L_\theta \cos(2\theta)}{3(L_d L_q)} & \dfrac{L_l + \dfrac{3}{2}L_{av} - 3L_\theta \cos\left(2\theta + \dfrac{2\pi}{3}\right)}{3(L_d L_q)} \\[4mm] \dfrac{-L_l - \dfrac{3}{2}L_{av} + 3L_\theta \cos\left(2\theta - \dfrac{2\pi}{3}\right)}{3(L_d L_q)} & \dfrac{L_l + \dfrac{3}{2}L_{av} - 3L_\theta \cos(2\theta)}{3(L_d L_q)} \end{bmatrix} \\[8mm] \left\{ \begin{bmatrix} v_{ab} \\ v_{bc} \end{bmatrix} - \begin{bmatrix} R + 6\omega_e L_\theta \sin(2\theta) & -R - 6\omega_e L_\theta \sin\left(2\theta + \dfrac{2\pi}{3}\right) \\[3mm] R + 6\omega_e L_\theta \sin\left(2\theta - \dfrac{2\pi}{3}\right) & 2R - 6\omega_e L_\theta \sin(2\theta) \end{bmatrix} \begin{bmatrix} i_a \\ i_b \end{bmatrix} \right. \\[6mm] \left. -\sqrt{3}\omega_e \lambda_m \begin{bmatrix} \sin\left(2\theta - \dfrac{5\pi}{3}\right) \\[3mm] \sin\left(\theta + \dfrac{\pi}{2}\right) \end{bmatrix} \right\} \end{Bmatrix} \qquad (46)$$

The torque equation in the stationary reference frame given by (11) along with (37-40) are used to develop the complete simulation environment for the PMSM, shown in Fig. 4.
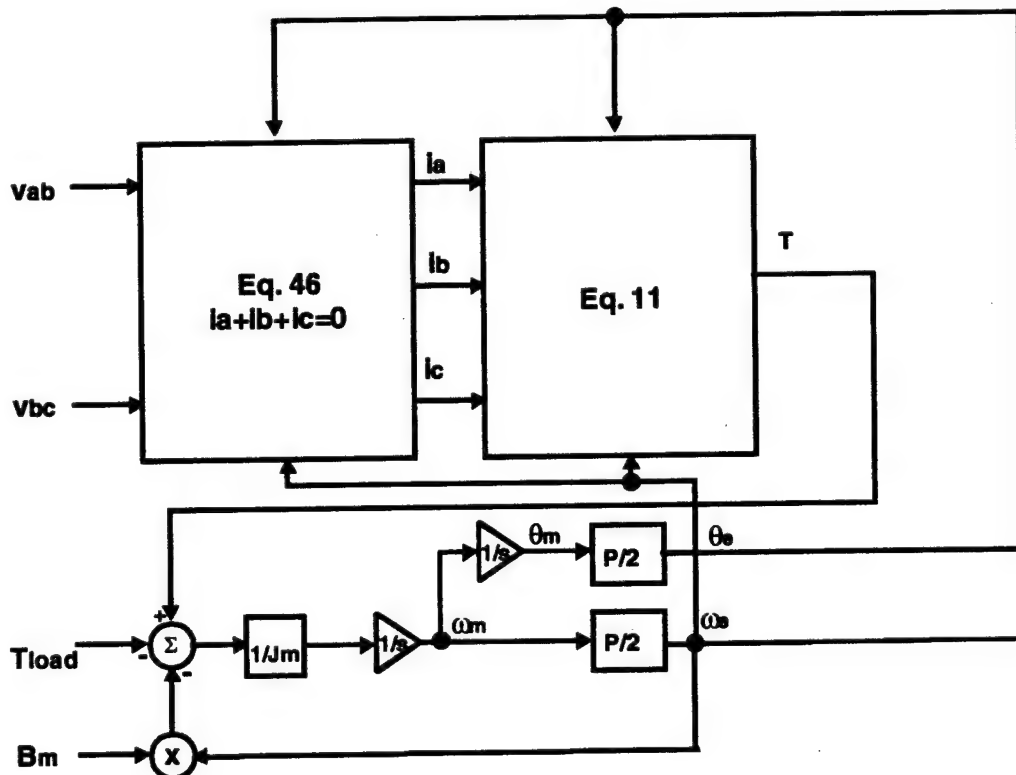

Fig. 4 Simulation model in stationary reference frame

3 ESTIMATION OF PMSM ROTOR POSITION AND SPEED

In this section, an implementation for sensorless operation of the PMSM is presented. The PMSM model is first decomposed into two linear systems so that linear control system design techniques may be applied to the observer design. The two resulting linear systems consist of the electrical and mechanical dynamics. The rotor position is estimated using a reference model and the measured phase currents and voltages corresponding to the electrical dynamics. A separate observer is used to estimate the rotor speed, corresponding to the mechanical (slow) dynamics.

3.1 Reference Model Decomposition

Under the assumption that the electrical time constant of the PMSM is much less that the mechanical time constant, the system is singularly perturbed [12], with the mechanical variables (ω_e, θ) evolving in a slow time scale with respect to the electrical variables.

The flux equations for the slotless PMSM in stationary coordinates were developed in chapter 2, and are given by (22). The equation is rearranged to yield

$$\frac{L}{R}\begin{bmatrix} \dot{\lambda}_\alpha \\ \dot{\lambda}_\beta \end{bmatrix} = -\begin{bmatrix} \lambda_\alpha \\ \lambda_\beta \end{bmatrix} + \sqrt{\frac{3}{2}}\lambda_m \begin{bmatrix} \cos\theta \\ \sin\theta \end{bmatrix} + \frac{L}{R}\begin{bmatrix} v_\alpha \\ v_\beta \end{bmatrix} \quad . \tag{47}$$

The mechanical variables are described in (37-40), which are summarized by:

$$\dot{\omega}_e = \frac{P}{2}\left(\frac{T - T_{load} - \frac{2}{P}B\omega_e}{J_m} \right) \tag{48}$$

and

$$\dot{\theta} = \omega_e \tag{49}$$

The electromechanical system described by 47-49 is clearly non-linear. The slow (mechanical) subsystem is represented by (48) and (49), while the fast (electrical) subsystem is given in (47). If we choose

$$x = \begin{bmatrix} \omega_e & \theta \end{bmatrix}^T \tag{50}$$

and

$$z = \begin{bmatrix} \lambda_\alpha & \lambda_\beta \end{bmatrix}^T, \tag{51}$$

then (47-49) can be written in the standard singular perturbation model :

$$\dot{x} = f(x,z,t) \ , x_s(t_0) = x^0$$
$$\varepsilon \dot{z} = g(x,z,t)$$

$$\quad,\quad \text{(52 a,b)}$$

where the scaling parameter $\varepsilon = L/R$ is small and greater than zero. To perform the time-scale decomposition, consider the case where the scaling parameter $\varepsilon \to 0$. In this case, the fast transient decays instantly, as long as it is an asymptotically stable system. This leaves the quasi steady-state model:

$$\dot{x}_s = f(x_s,z_s,t) \ , x_s(t_0) = x^0$$
$$0 = g(x_s,z_s,t)$$

$$\quad,\quad \text{(53 a,b)}$$

where the subscript s indicates the quasi steady-states in the slow time scale.

If a fast time scale is now introduced where

$$\tau = \frac{t-t_0}{\varepsilon}, \quad \tau = 0 \ \text{at} \ t = t_0 \ , \quad\quad \text{(54)}$$

then (52) can be written in the fast time scale as

$$\frac{dx}{d\tau} = \varepsilon f(x,z,t'+\varepsilon\tau)$$
$$\frac{dz}{d\tau} = g(x,z,t'+\varepsilon\tau)$$

$$\quad,\quad \text{(55 a,b)}$$

where the fixed instant t' is chosen to be t_0. Examining the limit as the scaling parameter $\varepsilon \to 0$ reveals that $dx/d\tau = 0$ and x is constant in the fast time-scale. Thus, the fast subsystem may be written as

$$\frac{dz_f}{d\tau} = g(x^0,z_s^0 + z_f(\tau),t_0) \ , z_f(0) = z^0 - z_s^0 \ , \quad\quad \text{(56)}$$

where x^0 and z_s^0 are fixed parameters. In the context of the PMSM, this result indicates that the electrical and mechanical subsystems may be separated. The slow mechanical variables are considered to be constant within the sampling interval of the fast electrical system.

In the design of a rotor position observer for the PMSM, the concept of time-scale separation is utilized. The concept of time-scale separation showed that if the machine's electrical time constant τ_e is small relative to the mechanical time constant τ_m then the rotor velocity is nearly constant in the fast time scale. Thus, if the sample period for the fast position observer is chosen to be short enough, the rotor velocity can be considered

to be a constant throughout the sample period. It is then possible to describe the system's behavior from one sample to the next by using a linear model that is a function of the rotor velocity. This approach suggests the use of two observers – a fast observer for rotor position estimation, and a slower one for the estimation of the angular velocity. These observers are presented in the following sections.

3.2   Full Order Observer for Estimation of Rotor Position

In this section, a PMSM fast model in the stationary two-phase reference frame is augmented to include the estimated states. From this partitioned model, a full order position observer is constructed. The full-order observer is selected over a reduced order implementation because of the beneficial smoothing of the estimated states that results. A reduced-order implementation would result in reduced computational requirements, but the performance tradeoffs of the two observer realizations were not investigated in this study.

Considering the fast electrical subsystem, the state vector of (51) can be augmented to include functions of the rotor angle. The augmented state vector is defined by

$$\mathbf{x} = [x_1 \ x_2 \ x_3 \ x_4]^T = [\lambda_\alpha \ \lambda_\beta \ \cos\theta \ \sin\theta]^T. \tag{57}$$

The input vector is the applied phase voltage in the stationary two-phase reference frame

$$\mathbf{u} = [u_1 \ u_2]^T = [v_\alpha \ v_\beta]^T, \tag{58}$$

and the output vector is chosen to be the measurable currents:

$$\mathbf{y} = [y_1 \ y_2]^T = [i_\alpha \ i_\beta]^T. \tag{59}$$

Thus, the state and output equations are

$$\dot{\mathbf{x}} = \mathbf{A}_\omega \mathbf{x} + \mathbf{Bu} \tag{60}$$
$$\mathbf{y} = \mathbf{Cx} \quad , \tag{61}$$

respectively, where

$$\mathbf{A}_\omega = \begin{bmatrix} -\tau & 0 & \sqrt{\frac{3}{2}}\lambda_m\tau & 0 \\ 0 & -\tau & 0 & \sqrt{\frac{3}{2}}\lambda_m\tau \\ 0 & 0 & 0 & -\omega_e \\ 0 & 0 & \omega_e & 0 \end{bmatrix}, \tag{62}$$

$$\mathbf{B} = \begin{bmatrix} 1 & 0 \\ 0 & 1 \\ 0 & 0 \\ 0 & 0 \end{bmatrix}, \tag{63}$$

$$\mathbf{C} = \begin{bmatrix} \dfrac{\tau}{R} & 0 & -\sqrt{\dfrac{3}{2}}\dfrac{\tau\lambda_m}{R} & 0 \\ 0 & \dfrac{\tau}{R} & 0 & -\sqrt{\dfrac{3}{2}}\dfrac{\tau\lambda_m}{R} \end{bmatrix}, \tag{64}$$

and
$$\tau = \frac{R}{L_l + \frac{3}{2}L_{ss}}. \tag{65}$$

The term ω_e represents the angular velocity of the rotor shaft in electrical radians per second. The subscript ω associated with the A matrix indicates that this matrix varies with the angular velocity of the rotor, and is therefore a time-varying system matrix. It is stressed that this model does not contain the mechanical variables such as torque, friction, and inertia in the state equations. This is advantageous, since torque and inertia are often unknown and vary during operation of the system.

3.2.1 Rotor Velocity Estimation

To develop an estimator for the angular velocity ω_e, the quasi steady-state (slow mode) electrical dynamic equation of (53b) is used. Allowing the time scale parameter ε to approach zero reveals, after some manipulations:

$$\sin\theta = \frac{Ri_\alpha - v_\alpha}{\sqrt{\frac{3}{2}}\omega_e\lambda_m} \tag{66}$$

and

$$\cos\theta = \frac{Ri_\beta - v_\beta}{\sqrt{\tfrac{3}{2}}\omega_e\lambda_m} . \tag{67}$$

In terms of space phasor notation, the above may be considered to be a rotating vector, and represented by

$$\sqrt{\frac{3}{2}}\omega_e\lambda_m e^{j\theta} = \left[(Ri_\alpha - v_\alpha) + j(Ri_\beta - v_\beta)\right] \tag{68}$$

so that the magnitude of the angular velocity is given by

$$|\hat{\omega}_e| = \frac{\left[(v_\alpha - Ri_\alpha)^2 + (v_\beta - Ri_\beta)^2\right]^{1/2}}{\sqrt{\tfrac{3}{2}}\lambda_m}, \tag{69}$$

and the direction is obtained from the direction of rotation of the back emf vector. At sampling interval k, the angle of the emf vector is given by

$$\theta_{emf}(k) = \tan^{-1}\left(\frac{Ri_\alpha(k) - v_\alpha(k)}{v_\beta(k) - Ri_\beta(k)}\right). \tag{70}$$

Thus, the estimated rotor speed magnitude is modified in sign based on the direction of rotation of the back emf vector, and the estimated velocity is

$$\hat{\omega}_e = \text{sgn}\left(\theta_{emf}(k) - \theta_{emf}(k-1)\right)|\hat{\omega}_e| . \tag{71}$$

Given the time scale separation, the estimated velocity $\hat{\omega}_e$ is calculated at a rate much slower than the rotor position estimator, since speed is considered to be a parameter in the position estimator algorithm. The rotor position estimator is described in the following section.

Alternatively, the rotor speed can also be estimated by differentiating the estimated rotor angle. The drawback to this method is the noise that results from the differentiation process. There are, however, some advantages to the use of this technique in combination with the method presented in this section. The modifications to the speed estimation method presented in this section are discussed in the implementation segment of this report.

3.2.2 Rotor Angle Observer

The PMSM equations of (57-65) correspond to the fast (electrical) mode of the time scale decomposed system, and are now used to design the rotor position observer for the sensorless PMSM drive. It is desired to estimate the state vector **x** of (57) from knowledge of the input vector **u** defined in (58) and direct measurement of the output vector **y** of (59). To achieve this, a full order observer is used due to the beneficial smoothing effects that result. Note that if x_3 and x_4 of (57) are estimated, the estimated rotor position $\hat{\theta}$ may be calculated by using the relation

$$\hat{\theta} = \tan^{-1}\left(\frac{\hat{x}_4}{\hat{x}_3}\right). \tag{72}$$

Using standard observer design techniques for a linear system [13], the form of the proposed observer is

$$\dot{\mathbf{e}} = (\mathbf{A}_\omega - \mathbf{GC})\mathbf{e} , \tag{73}$$

where **e** is the state estimation error vector,

$$\mathbf{e} = \mathbf{x} - \hat{\mathbf{x}} , \tag{74}$$

and **G** is the observer gain matrix. Under the previous assumption that rotor velocity ω_e is approximately constant over the sample period of the position observer, the system is linear over that period and observable for non-zero rotor velocities. Fig. 5 shows the structure of the resulting observer.

Each time a new velocity estimate is available, the observer gain matrix **G** is calculated by using conventional pole-placement methods [13]. With this technique, the eigenvalues of the characteristic equation

$$|s\mathbf{I} - (\mathbf{A}_\omega - \mathbf{GC})| = 0 \tag{75}$$

are placed in the left-half plane at locations such that the observer estimation error **e** converges to zero within a satisfactory period of time. Note that the observer gain matrix **G** is dependent on the rotor velocity, the desired eigenvalues, and the PMSM parameters. In practice, the eigenvalues of the position observer should always be selected such that the position estimation error converges at a fast rate with respect to the rotor speed ω_e. Thus, the gain scheduler in the prototype sensorless PMSM drive selects the observer gain matrix values based on the estimated rotor velocity. The gain matrix is updated at

the same rate as the velocity estimates. In the DSP implementation, the digital controller is constructed from the continuous-time observer equations presented above using the forward Euler integration method.
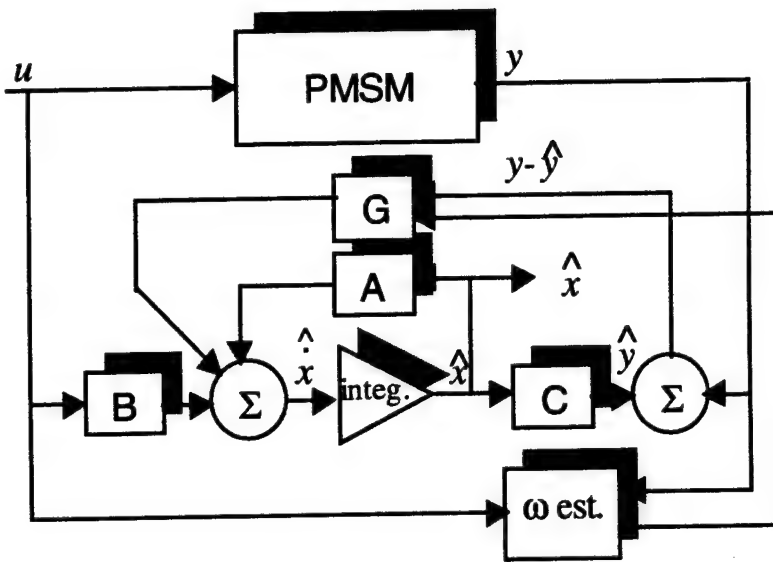

Fig. 5 Block diagram of rotor position estimator

A will known drawback of the sensorless drive is its inability to estimate rotor angle at zero speed. This difficulty can be clarified through use of the PMSM model. From the model, the condition for rotor position observability at zero speed is not met since the observability matrix

$$
\begin{bmatrix} \mathbf{C} \\ \mathbf{CA}_\omega \\ \mathbf{CA}_\omega^2 \\ \mathbf{CA}_\omega^3 \end{bmatrix},
\tag{76}
$$

is not full rank for $\omega_m = 0$. In the above, $\mathbf{A}_\omega$ and $\mathbf{C}$ are defined in (62) and (64), respectively. Thus, in the absence of a zero-speed rotor position estimation technique, special provisions must be made to start the sensorless PMSM from zero speed.

In the prototype sensorless PMSM drive, the rotor position estimation difficulties at zero and low speed are managed by setting the observer gain matrix $\mathbf{G}$ to zero for angular velocities below some low-speed threshold. This essentially disables the observer, and under such conditions the internal PMSM model runs without correctional feedback. This technique has been shown to be effective for short time periods of low-speed operation such as during a speed reversal. During a reversal of speed, the open loop model is effective in providing the position estimate until rotor speed is reversed and its

21

magnitude is above the low-speed threshold. At this point, observer correction is restored. Test results for speed reversals are included in section 5.3.2.

For startup from zero speed, however, a method is used where the sensorless drive ramps the machine to the threshold speed, at which point the sensorless algorithm assumes control. The low-speed threshold for the prototype sensorless drive was selected by experimentation to be approximately 1.5 Hz, which corresponds to 23 RPM for the 8 pole slotless PMSM.

4 SENSORLESS DRIVE IMPLEMENTATION

In this chapter, the sensorless strategy developed in Chapter 3 is implemented in a closed-loop drive system. The algorithm is implemented on a digital signal processor (DSP). Although many sensorless control algorithms have been proposed in literature, there have been very few that actually demonstrate the performance of the drive in a closed-loop experiment. Therefore, some issues that were encountered during the implementation and experimentation process are described.

4.1 Data Acquisition

This section describes some real-time implementation issues associated with data acquisition for the rotor position observer presented in Chapter 3. As depicted in Fig. 5, the rotor position observer relies on the measurement of stator voltages and currents, making it necessary to pay close attention to the acquisition of these signals. Any infidelity in these measurements will have a detrimental effect on the rotor angle estimation accuracy. The acquisition of high quality measurements in the PWM drive environment is not a trivial undertaking.

The prototype sensorless drive system uses a 12-bit flash A/D converter with simultaneous sampling capability synchronized to the PWM frequency. Simultaneous sampling is an important feature that provides a snapshot of the stator variables at the sampling instant. Synchronized sampling to the PWM frequency will be shown to be beneficial toward accurate rotor position estimation.

4.1.1 Voltage Measurement

The use of the PWM inverter is nearly universal in PMSM drives, making accurate voltage measurements problematic due to the switching nature of the applied phase voltage. Often, the applied phase voltages are computed using a combination of the DC link voltage and the commanded PWM duty cycles. Another approach is to apply a low-pass filter to the phase voltage to remove the high frequency PWM switching component, but leaving the fundamental component of interest. In this section, implementations pertaining to both strategies are discussed. Comparisons of these two methods in terms of rotor position estimation accuracy are presented in the experimental results section of this document.

4.1.1.1 Indirect Phase Voltage Measurement through PWM Reference Command

To obtain the phase voltage of a PMSM, the commanded voltage reference to the PWM inverter is often used as an approximation. The main drawback to this approach is that due to inverter non-idealities, the actual phase voltage does not match the commanded value. The two most significant of these non-ideal characteristics are the PWM deadtime effects, and the voltage drops across the conducting components in the inverter.

PWM deadtime (illustrated in Fig. 7 as t_d) is a necessary delay imposed on the PWM gate signals in each inverter leg such that the two switches in that leg (*sa* and *sa'* in Fig. 7) are never simultaneously in the conducting state. This condition would result in damaging "shoot-through" currents. In addition to the PWM deadtime effects, the power switching stage exhibits voltage drops in the transistors and flyback diodes – both of which are shown in Fig. 6. These voltage drops generally increase with the current level [14]. Based on these non-ideal inverter characteristics, it is clear that in order to use the voltage reference method to obtain an accurate indication of the actual phase voltage, the deadtime effects and voltage drops in the inverter devices must be accounted for.

In general, it is possible to compensate for the inverter output voltage distortion through the use of feedforward techniques [15,16]. In using such techniques, the commanded PWM duty cycle values are adjusted to compensate for the non-idealities of the inverter. It is the objective of this section to introduce a technique for synthesis of PMSM phase-to-neutral voltage such that the voltage reference is a very close representation of the actual phase to neutral voltage. Thus, the voltage reference signals may be used as the input vector for the rotor position estimator.

The requirement for a phase-neutral voltage synthesis strategy may best be illustrated by considering the inverter shown in Fig. 6. This inverter structure, which is typically used to drive a PMSM, translates the PWM reference command signals (*sa*, *sa'*, *sb*, *sb'*, *sc*, and *sc'*) from the control logic to the appropriate high voltage levels. If the inverter contained perfect switches, then the voltages applied to the motor could be determined exactly from the DC link voltage ($V^+ - V^-$) and the PWM reference signal duty cycles. In a more realistic PWM inverter, however, the aforementioned sources of distortion would result in an error between the voltage command and the actual inverter output voltage. A voltage synthesis method that accounts for the inverter non-idealities is presented in the following paragraphs.
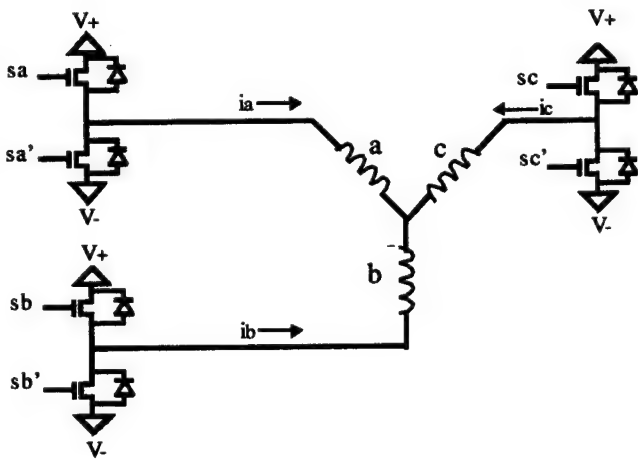

Fig. 6 PMSM inverter
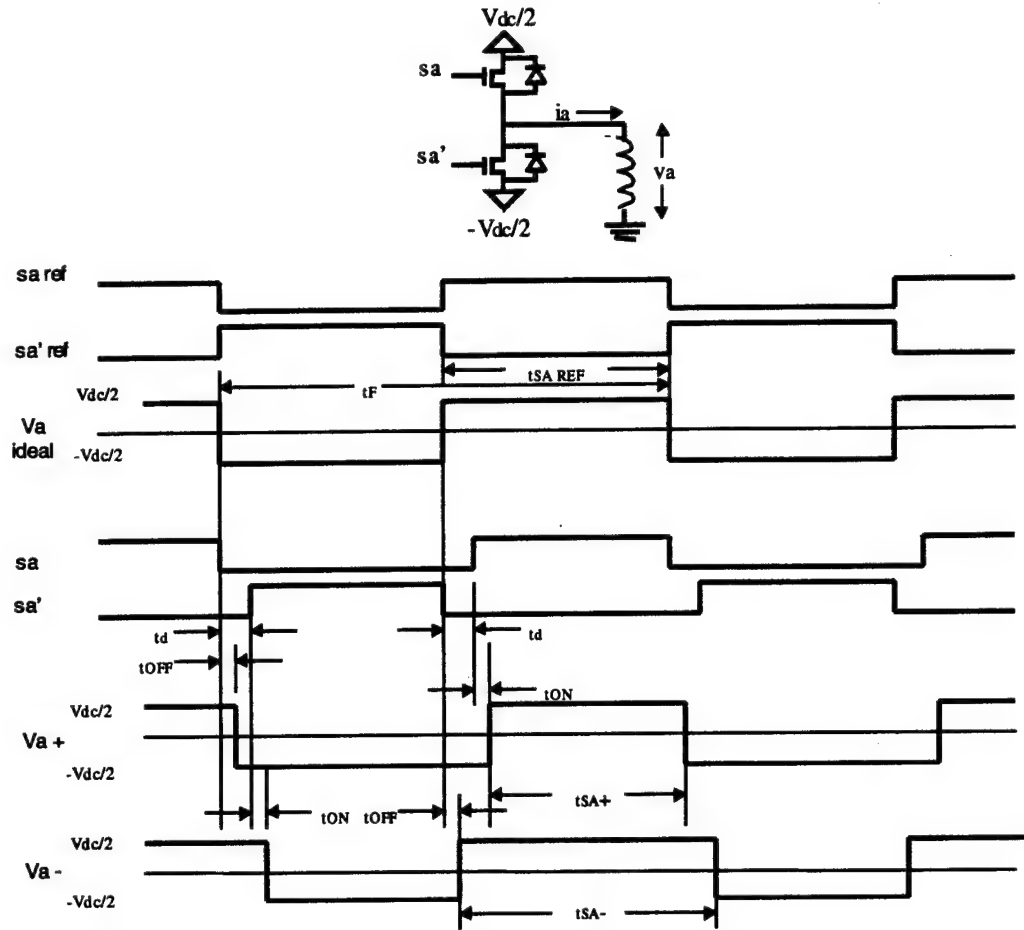
Fig. 7 Signal and timing diagram for single phase of voltage source inverter

To examine the effects of PWM deadtime, consider a single leg (phase *a*) of the PWM inverter in Fig. 7. The duty cycle of the voltage reference signals (sa_{ref}, sa'_{ref}) represent the switching signal required to apply the desired (ideal) average voltage to the phase winding. However, a deadtime is introduced to these PWM reference signals to yield the dead-time compensated PWM voltage references (*sa*, *sa'*). Dead-time compensation is often implemented by adding a delay t_d to the power switch that is turning on. Therefore, the actual deadtime compensated duty cycle commands apply the voltages V_{a+} or V_{a-} to phase *a* for positive and negative load currents i_a, respectively. The effective on time of the resulting voltage signals V_{a+} and V_{a-} are represented by t_{sa+} and t_{sa-}, respectively. Clearly, the intended terminal voltage $V_{a\,ideal}$ has not been produced at the terminals. The figure shows how both the load current direction i_a and the deadtime effects modify the effective on time t_{sa+} or t_{sa-} from its ideal value $t_{sa\,ref}$.

The reason load current direction has an effect on the average terminal voltage is that during the deadtime t_d, switches *sa* and *sa'* do not conduct, and one of the two flyback diodes is turned on. The diode that conducts during the deadtime is determined by the

25

direction of the load current i_a. Therefore, from the structure of the inverter, either $v_{dc}/2$ or $-v_{dc}/2$ will be applied to the terminal during the deadtime.

From Fig. 7, the effective on time t_{sa} of the system can be identified by comparing the ideal inverter output voltage $V_{a\,ideal}$ with the actual inverter output voltage (v_{a+} and v_{a-}). For positive load current, comparison of t_{sa+} and t_{saref} in Fig. 7 shows that the effective on time is

$$t_{sa} = t_{saref} + (t_{off} - t_{on} - t_d), \qquad (77)$$

where t_{on} and t_{off}, t_{aref}, and t_d represent the turn-on and turn-off delays of the power switching device, commanded on-time of the phase voltage, and deadtime of the inverter, respectively. Similarly, for a negative load current, the effective on time is

$$t_{sa} = t_{saref} - (t_{off} - t_{on} - t_d). \qquad (78)$$

The above results may be extended to all phases of the inverter, and written in a more general form:

$$t_{sx} = t_{xref} + sign(i_x)T \quad \text{for } x = \{a,b,c\}, \qquad (79)$$

where

$$T = (t_{off} - t_{on} - t_d), \qquad (80)$$

and

$$sign(i_x) = \begin{cases} 1 \text{ when } i_x > 0 \\ -1 \text{ when } i_x < 0 \end{cases}. \qquad (81)$$

From (79), the effective on time t_{sx} of the actual inverter output differs from the commanded on-time by T.

In addition to the deadtime effect considered above, there exists a voltage drop in the components of the inverter that generate yet another distortion between the commanded and actual voltage. To analyze this effect, all three phases must be considered since the phase-to-neutral voltages are a coupled system. The system under consideration is shown in Fig. 8.

Considering phase x of the Fig. 8 where $x = \{a,b,c\}$, if the current i_x is positive, the actual voltage from the inverter phase output to ground will be

$$v_{xg} = \frac{v_{dc}}{2} - v_t \quad \text{when } sx \text{ is on}, i_x \text{ positive} \tag{82}$$

and

$$v_{xg} = -\frac{v_{dc}}{2} - v_d \quad \text{when } sx \text{ is off}, i_x \text{ positive.} \tag{83}$$

The state of switch sx is considered to be on when the upper conductor (sx) in the inverter leg x is conducting and the lower leg (sx') is non-conducting. The terms v_{dc}, v_t and v_d represent the DC link voltage, and voltage drops in the transistor switching device and flyback diodes, respectively.

When the phase x current is negative, the actual voltage now becomes

$$v_{xg} = \frac{v_{dc}}{2} + v_d \quad \text{when } sx \text{ is on}, i_x \text{ negative} \tag{84}$$

and

$$v_{xg} = -\frac{v_{dc}}{2} + v_t \quad \text{when } sx \text{ is off}, i_x \text{ negative .} \tag{85}$$
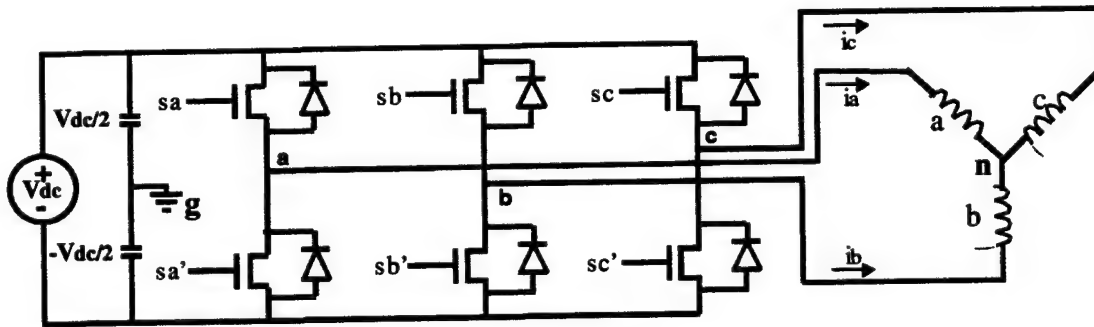

Fig. 8. PMSM Inverter model for phase voltage synthesis

Equations (82-85) may now be written in a more compact form:

$$v_{xg} = -\frac{1}{2} sign(i_x)(v_t + v_d) + \left(sx - \frac{1}{2}\right)(v_{dc} - v_t + v_d) , \tag{86}$$

where the symbol sx is equal to one if the upper transistor in the inverter leg of phase x is on, and zero otherwise. Recognizing that the average effective value of sx over a PWM cycle is proportional to the effective on time divided by the PWM period t_f, the average phase-to-ground voltage on phase x during a PWM cycle can now be represented by

$$v_{xg} = -\frac{1}{2} sign(i_x)(v_t + v_d) + \left(\frac{t_{sx}}{t_f} - \frac{1}{2}\right)(v_{dc} - v_t + v_d) . \tag{87}$$

The model presented for the PMSM requires knowledge of the phase-to-neutral voltages v_{xn}. These may now be obtained by recognizing that for a PMSM with a buried neutral, no zero-sequence currents may flow (eq. 41). In addition, for a symmetric machine and load, the neutral voltages are constrained as well so that

$$v_{an} + v_{bn} + v_{cn} = 0. \tag{88}$$

From Fig. 8, it is simple to see that the phase-to neutral voltages are

$$v_{xg} = v_{xn} + v_{ng} . \tag{89}$$

Now, with the help of eq. (88), we can write

$$\sum_{x=a,b,c} v_{xg} = 3v_{ng} . \tag{90}$$

Using (87) and (90), the PMSM neutral to bus voltage ground can be determined:

$$v_{ng} = -\frac{1}{6}\left(\sum_{x=a,b,c} sign(i_x)\right)(v_t + v_d) + \frac{2\sum_{x=a,b,c} t_{sx} - 3t_f}{6t_f}(v_{dc} - v_t + v_d) . \tag{91}$$

Finally, equations (87), (89), and (91) allow for the calculation of the desired line-neutral voltages in terms of the deadtime compensated PWM reference signals:

$$v_{xn} = \frac{v_t + v_d}{6}\left(\sum_{y=a,b,c} sign(i_y) - 3sign(i_x)\right) + \frac{v_{dc} - v_t + v_d}{3t_f}\left(3t_{sx} - \sum_{y=a,b,c} t_{sy}\right). \tag{92}$$

The above equation can be put into matrix form and expressed in terms of the commanded duty cycle t_{sxref} by using (79):

$$\begin{bmatrix} v_{an} \\ v_{bn} \\ v_{cn} \end{bmatrix} = \frac{v_{dc} - v_t + v_d}{3t_f}\begin{bmatrix} 2 & -1 & -1 \\ -1 & 2 & -1 \\ -1 & -1 & 2 \end{bmatrix}\begin{bmatrix} t_{saref} \\ t_{sbref} \\ t_{scref} \end{bmatrix}$$
$$+ \frac{\left((v_{dc} - v_t + v_d)\dfrac{2T}{t_f} - v_d - v_t\right)}{6}\begin{bmatrix} 2 & -1 & -1 \\ -1 & 2 & -1 \\ -1 & -1 & 2 \end{bmatrix}sign\begin{bmatrix} i_a \\ i_b \\ i_c \end{bmatrix} \tag{93}$$

The matrix form shows that there is not a unique solution for the reference duty cycle commands t_{sxref}, since the matrix

$$\begin{bmatrix} 2 & -1 & -1 \\ -1 & 2 & -1 \\ -1 & -1 & 2 \end{bmatrix}$$

is singular. Thus, a constraint is required to obtain a solution. In order to maintain the average PMSM neutral voltage at ground potential, eq. (91) is solved while setting $v_{ng} = 0$. This results in a constraint for the sum of the effective PWM duty cycles:

$$\sum_{y=a,b,c} t_{sy} = \frac{(v_t + v_d)t_f \sum_{y=a,b,c} sign(i_y)}{2(v_{dc} - v_t + v_d)} + \frac{3}{2}t_f . \tag{94}$$

The constraint of eq. (94) allows eq. (92) to be solved for the duty cycle command to achieve the desired phase-to-neutral voltage. Inserting (94) into (92) yields:

$$v_{xn} = -\frac{v_t + v_d}{2} sign(i_x) + (v_{dc} - v_t + v_d)\frac{t_{sx}}{t_f} - \frac{(v_{dc} - v_t + v_d)}{2}. \tag{95}$$

This can be re-written in terms of the commanded PWM duty cycle t_{sxref} by using eq. (79), which gives

$$v_{xn} = \frac{(v_{dc} - v_t + v_d)}{t_f}t_{sxref} - \frac{v_t + v_d}{2} sign(i_x) + \frac{T(v_{dc} - v_t + v_d)}{t_f} sign(i_x) - \frac{(v_{dc} - v_t + v_d)}{2}. \tag{96}$$

Eq. (96) relates the reference PWM duty cycle command t_{sxref} to the actual phase x to neutral voltage. It stands to reason that if a commanded voltage v_{xn}^* is desired at the inverter output, we can solve (96) for the required duty cycle command to achieve this voltage:

$$t_{sxref} = \left(\frac{v_{xn}^*}{v_{dc} - v_t + v_d} + \frac{1}{2}\right)t_f + \left(\frac{(v_t + v_d)t_f}{2(v_{dc} - v_t + v_d)} - T\right)sign(i_x). \tag{97}$$

This is the desired result since the desired phase voltage, typically generated by the current control loop, can be used to calculate the pre-deadtime compensated PWM duty cycle required to apply the commanded phase voltage to the PMSM. This technique allows the phase voltage commands to be used as the input to the rotor position observer as an alternative to instrumenting each phase winding with the appropriate measurement

electronics. Note, however, that with the DC bus voltage v_{dc} must still be measured. The advantage of this technique as compared to the direct measurement of the phase voltages is the avoidance of the low pass filtering typically associated with the latter method. In addition, the direct phase voltage measurement method tends to increase system cost and complexity.

4.1.1.2 Direct Measurement of Phase Voltage

To measure inverter output voltages directly, electrical isolation is typically required. In addition, low-pass filtering is essential to remove the high frequency switching signals generated by the PWM process, while allowing the fundamental component of the phase voltage to pass. The advantage of the direct measurement technique is that inverter deadtimes and non-ideal characteristics of the inverter components are inherently accounted for, since the actual phase voltage is measured.

A block diagram of the configuration used to directly measure the phase voltage is shown in Fig. 9. In the figure, both the PMSM and the resistive divider network (R_1 and R_2) are assumed to be symmetric so that the voltage between the PMSM neutral and the *false* neutral (abbreviated fn in Fig. 9) can be expressed as

$$v_{n-fn} = -v_{an} + v_{afn} \qquad (98\ a)$$

$$v_{n-fn} = -v_{bn} + v_{bfn} \qquad (98\ b)$$

$$v_{n-fn} = -v_{cn} + v_{cfn} \quad . \qquad (98\ c)$$

In addition, due to the symmetry

$$v_{an} + v_{bn} + v_{cn} = 0 \qquad (99a)$$

$$v_{afn} + v_{bfn} + v_{cfn} = 0 \qquad (99b)$$

Summing the three relations for the neutral to false neutral voltage reveals that the voltage between the two neutrals is zero:

$$3v_{n-fn} = -\left(v_{an} + v_{bn} + v_{cn}\right) + \left(v_{afn} + v_{bfn} + v_{cfn}\right) = 0 \ . \qquad (100)$$

With the false neutral at the same voltage potential as the buried PMSM neutral connection, it can be seen in Fig. 9 that the voltage applied to the low pass filter is the scaled phase-to-neutral PMSM voltage. The resistive divider is used to scale this voltage to levels compatible with the analog filters and amplifiers used in the sensorless drive.

The major drawback to this technique is that the low-pass filter introduces a phase shift such that high frequency measurement fidelity is compromised. This phase shift is detrimental to the performance of the rotor position estimator, which requires accurate phase voltage measurements.
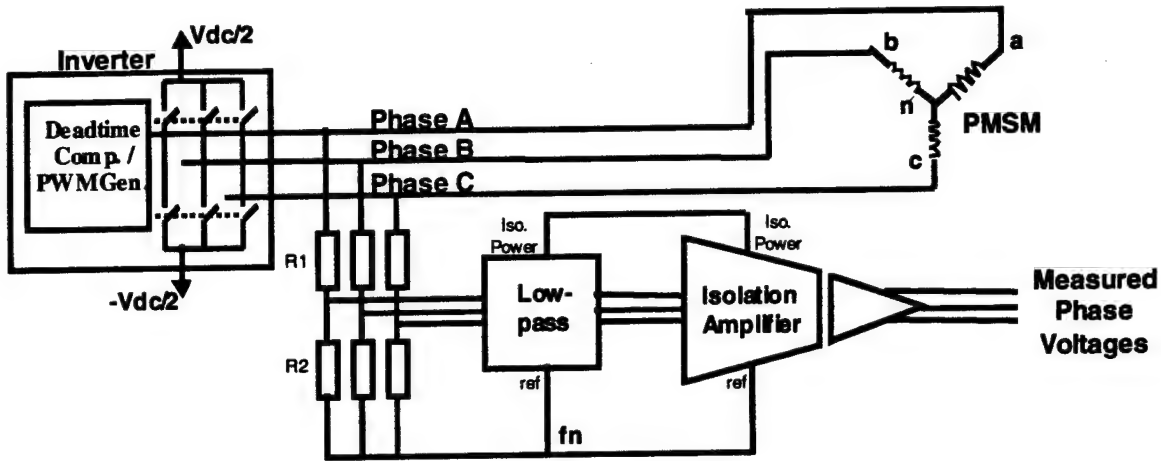
Fig. 9 Instrumentation for direct measurement of phase voltage

4.1.2 Current Measurement

In this section, the attention is focused on the acquisition of the stator currents. As in most servo control applications, the sensorless drive requires synchronous sampling of two motor currents. The current of the third phase is derived from the two measured values.

In a PWM driven current controller, the current waveform can contain higher frequency components than the sampling frequency. In the case of the sine-carrier comparison PWM or space-vector PWM schemes [17], the harmonic frequencies are multiples of the reference (dither) signal [18]. To filter these frequencies, a low-pass filter is often used before sampling the signal. This introduces an undesired delay.

Sampling the current synchronously with the PWM waveform relieves this situation by reducing the effect of PWM ripple on the sampled data. In doing so each of the sideband harmonics are symmetric about the PWM switching frequency harmonic. By sampling at the PWM switching frequency, all of the sideband harmonics sum to DC. Furthermore, by sampling at the zero mean point of the current ripple, the sideband harmonics sum to zero. This zero mean point of the current aligns with the peak of the PWM dither signal of a center-based PWM system, or equivalently at the center of the on-time illustrated in Fig. 10. For a center-sampled system, there is a single axis of symmetry for all three waveforms at the midpoint of the PWM cycle. This is the optimum point to sample current, since there is no switching here, and the current is at its average value.

For purposes of comparison, Fig. 11 shows the actual current generated by a PWM inverter beside both synchronously and asynchronously sampled phase currents. For the synchronously sampled case, where the current was sampled in the center of the PWM cycle, it is seen that the average phase current results. In the case of an asynchronously sampled current, significant ripple results in the sampled signal.

31
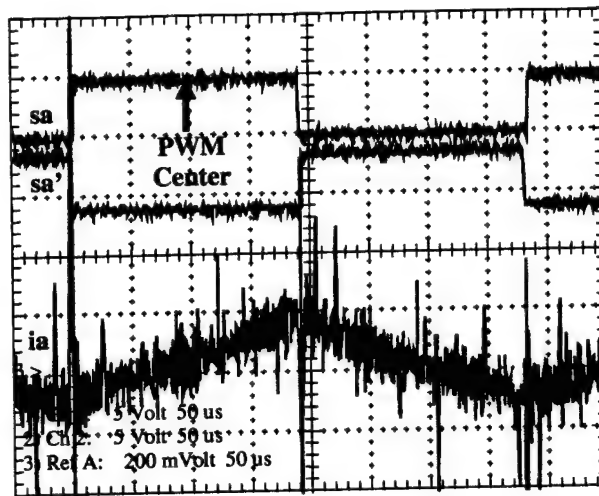
Fig. 10 PWM control signals (*sa*, *sa'*) and resulting phase current
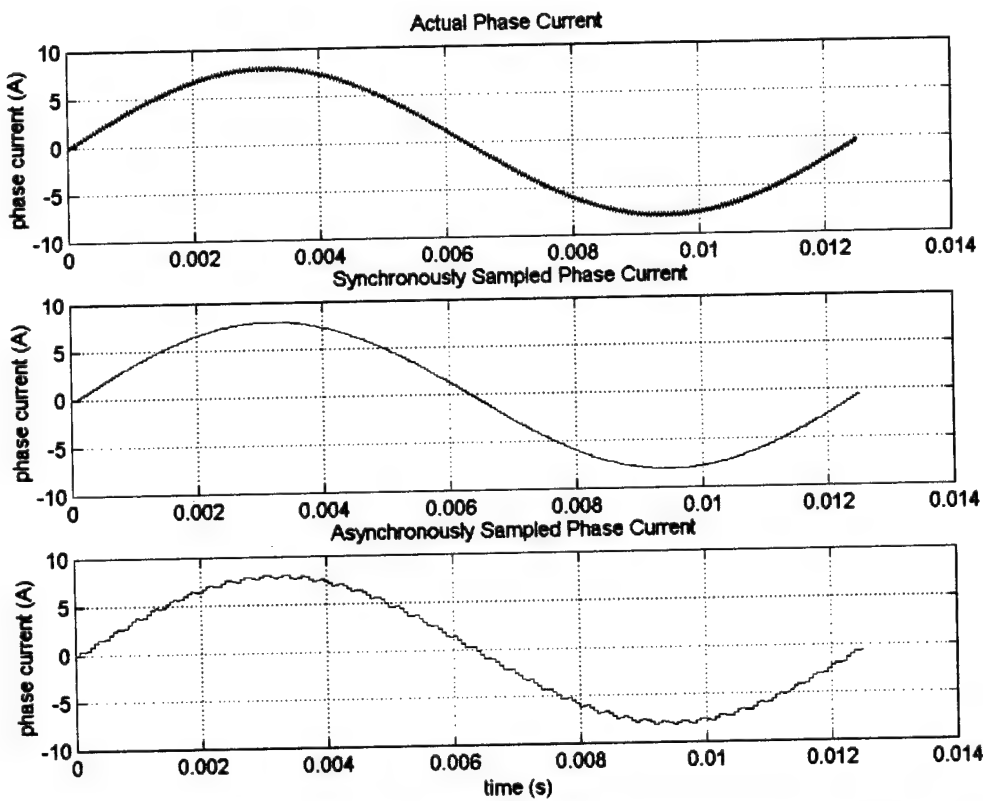
Fig. 11 Actual, synchronously sampled, and asynchronously sampled phase current waveforms

Fig. 12 shows the effect of shifting the sampling point in a synchronously sampled system. Center sampling results in the average current, while the other choices yield a current waveform containing an offset. This current offset is undesirable for several reasons. In addition to its adverse effect on the rotor position observer, it has been shown

that offsets in current sensors result in torque oscillations at the electrical frequency of the PMSM [19]. In the prototype sensorless drive, both voltage and current are simultaneously sampled at the PWM center point.
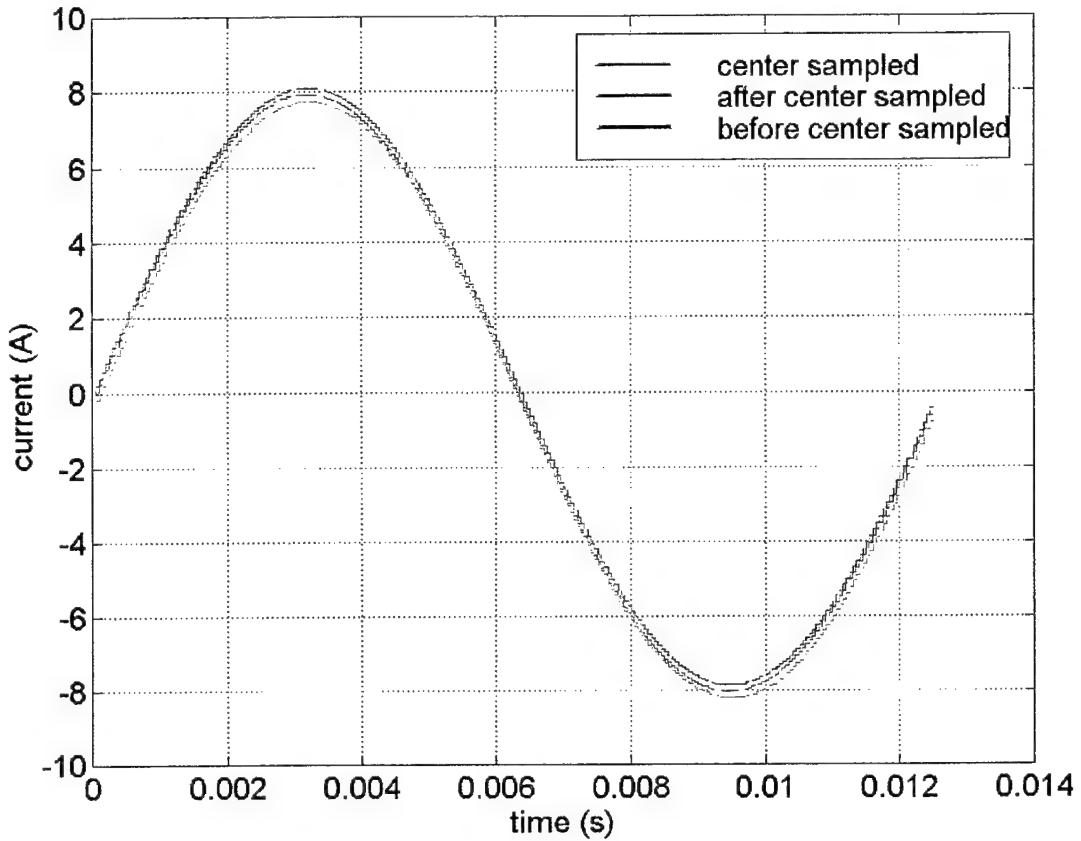
Fig. 12 Effect of current sampling point in a synchronously sampled system.

4.2 PMSM Control

This section describes the implementation of both a current and velocity controller for the prototype sensorless PMSM drive. The current controller is developed in the rotating reference frame derived from the estimated rotor position. The velocity controller for the sensorless drive is implemented such that parameter uncertainty does not result in velocity inaccuracies in the steady state. Current and velocity control are implemented as cascaded loops based on the time scale decomposition introduced in section 3.

4.2.1 Current Control

There have been several strategies proposed for current control of the PMSM. Some of these methods include hysteresis control [20], stationary frame proportional-integral (PI) control [21], and rotating reference frame PI control [22]. Of these, the latter has been acknowledged as being superior as it allows a fixed switching frequency and, unlike the

stator-frame PI control, allows zero control error at steady state. In the rotating reference frame current control is greatly simplified, making a three-phase machine equivalent to analyzing a DC motor. Thus, the current controller operates on DC quantities, and can in theory regulate the currents with zero steady-state error. In the stator reference frame, however, the current regulator operates on AC quantities corresponding to the motor speed, and is not able to achieve zero steady-state error.

Due to the computational burden of executing current control in the rotating reference frame, however, the current loop of PMSM servo drives has traditionally been performed with analog components in the stationary reference frame. More recently, the processing power and low price of the modern DSP has allowed the implementation of entirely digital current controllers for the PMSM drive in the rotating reference frame.

The current controller for the prototype sensorless drive is designed to operate in the rotating reference frame fixed to the estimation angle. For a small rotor angle estimation error, the estimated and actual rotor reference frames coincide, and the machine model given in (33) can be used to develop a suitable current controller. Eq. (33) is re-written for convenience:

$$v_d = L_d \frac{di_d}{dt} + Ri_d - \omega_e L_q i_q \tag{101}$$

$$v_q = L_q \frac{di_q}{dt} + Ri_q + \omega_e L_d i_d + \sqrt{\frac{3}{2}}\omega_e \lambda_m \quad . \tag{102}$$

The design of a rotating (synchronous) reference frame current controller for the sensorless PMSM is now developed. The current loops are based on a machine back emf model with a proportional-integral (PI) error loop. From (101) the direct axis current controller shows a cross coupling proportional to the product of the quadrature axis current and rotor speed. Similarly for quadrature axis current control (102) there are two disturbances: the cross-coupling of the direct axis current and the back-emf term. The term $\sqrt{3/2}\lambda_m \omega_e$ represents the back emf in the fictitious quadrature axis coil.

In this design the cross-coupling and back-emf terms evident in (101-102) are eliminated by a decoupling arrangement, while the transient response is improved through use of a feedforward term. In the ideal case where the PMSM parameters are exactly known, the feedforward and cross-coupling terms could be used to produce exactly the required output voltage for accurate current tracking. In such a case, the output of the current controller at sampling instant k would be

$$\mathbf{v}_{dq}^*(k) = \mathbf{v}_{dq}^{ff}(k) + \mathbf{v}_{dq}^{\omega}(k) \tag{103}$$

where $\mathbf{v}_{dq}^{ff}$ and $\mathbf{v}_{dq}^{\omega}$ are the feedforward and decoupling vectors, respectively. The feedforward and decoupling vectors may be written with the help of (101-102):

$$\mathbf{v}_{dq}^{ff}(k) = \frac{1}{T_s}\begin{bmatrix} L_d & 0 \\ 0 & L_q \end{bmatrix}\left[\mathbf{i}_{dq}^*(k) - \mathbf{i}_{dq}^*(k-1)\right] + R\left[\mathbf{i}_{dq}^*(k)\right] \tag{104}$$

and

$$\mathbf{v}_{dq}^{\omega}(k) = \begin{bmatrix} 0 & -\hat{\omega}_e L_q \\ \hat{\omega}_e L_d & 0 \end{bmatrix}\left[\mathbf{i}_{dq}(k)\right] + \sqrt{\frac{3}{2}}\hat{\omega}_e \lambda_m \begin{bmatrix} 0 \\ 1 \end{bmatrix} , \tag{105}$$

where T_s and i_{dq}^* are the sampling time and current references, respectively. The decoupling vector $\mathbf{v}_{dq}^{\omega}$ is used to overcome the rotor velocity-dependent cross coupling and motor back emf terms. Note that in the sensorless drive, the estimated rotor velocity must be used as indicated in (105). The feedforward term estimates the voltage reference required to overcome the passive voltage drops in the PMSM. Thus, it is seen that the current controller output represents the voltage required to force the actual stator currents to track the reference.

In reality, the current control structure of (103) is not sufficient for good current tracking because of the unavoidable effects of disturbances and PMSM parameter uncertainties. Thus, a PI controller term is added to the current control structure of (103) to yield the current control law

$$\mathbf{v}_{dq}^*(k) = \mathbf{v}_{dq}^{PI}(k) + \mathbf{v}_{dq}^{ff}(k) + \mathbf{v}_{dq}^{\omega}(k) , \tag{106}$$

where $\mathbf{v}_{dq}^{PI}$ is the PI controller output vector. The inclusion of the PI regulator allows for robustness despite the unavoidable modeling inaccuracies. Using impulse invariance to discretize the PI controller yields the difference equation

$$v_{dq}^{PI}(k) = v_{dq}^{PI}(k-1) + (K_P + K_I)\left[\mathbf{i}_{err-dq}(k) - \frac{K_P}{K_P + K_I}\mathbf{i}_{err-dq}(k-1)\right] , \tag{107}$$

where $\mathbf{i}_{err-dq}$ is the current error vector

$$\mathbf{i}_{err-dq}(k) = \mathbf{i}_{dq}^*(k) - \mathbf{i}_{dq}(k-1). \tag{108}$$

The proportional and integral gains K_p and K_I are selected to be equal in the d and q axis current controllers, and are determined experimentally to give a closed loop current controller of sufficient bandwidth (typically on the order of 1 KHz or greater).

A functional block diagram of the current control used on the prototype sensorless drive is shown in Fig. 13. In a velocity control application, an outer velocity controller

generates the current or torque command i^*, which is translated to d-q current commands by the reference current generator. The direct axis current reference i_d^* is normally maintained at zero, since from (36), direct axis current does not produce torque in a non-salient PMSM. The quadrature axis current command i_q^* represents the primary torque-producing component.

In Fig. 13, the feedback currents are transferred into the rotating reference frame through the Park and Clarke transforms (30) and the rotor angle, which is generated by the rotor position estimator. Comparison of the current reference to the feedback yields the current error, which is compensated by the PI controller to generate the voltage references in the rotating reference frame. Finally, the voltage reference is transformed to voltage commands in the stationary frame, which are operated on by the PWM controller to generate the inverter switching control signals. Only two current values are measured by the DSP since the third phase current not an independent variable for a Y connected PMSM.
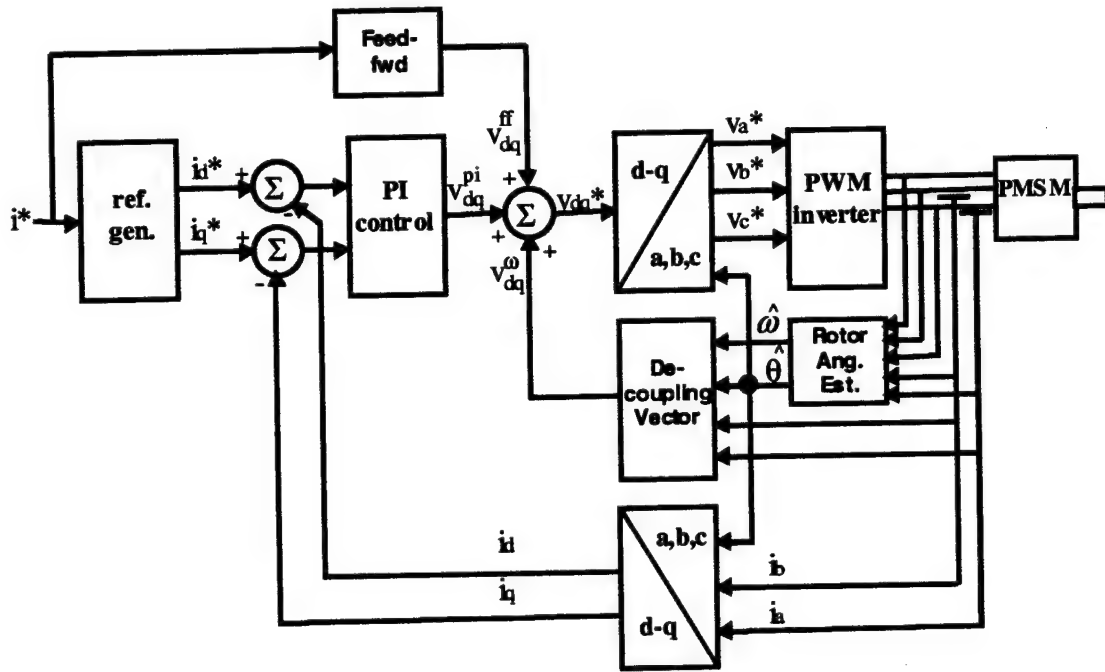
Fig. 13 Current control block diagram in the rotating reference frame

4.2.2 Velocity Control

In order to accurately control PMSM shaft velocity, accurate rotor velocity feedback is required. In a sensorless application, however, only a velocity estimate is available for this purpose. For the angular velocity estimation technique developed in section 3.2.1, the velocity estimate (69) is inversely proportional to the temperature-dependent permanent

magnet flux linkage λ_m. Therefore, the use of this estimate as the velocity feedback would result in velocity estimation error in situations where there is some parameter uncertainty. For Neodymium magnets used in high performance PM machines, the PM flux linkage parameter may be reduced by over 20 percent as the temperature varies from $-40°$ to $150°$ Celsius [23]. Thus an adaptive velocity control method is required to assure accurate tracking of the velocity reference signal.

For the sensorless system, this issue was addressed by using the time derivative of the estimated rotor angle to correct the velocity estimate of (69). Over a sufficient time period, the average time derivative of the rotor position estimate is equal to the actual rotor velocity as long as the rotor position estimator is stable. To achieve velocity estimate correction, the estimate of (69) is modified to include the term Δ, which represents the uncertainty in the permanent magnet flux linkage parameter λ_m:

$$\left|\hat{\omega}_e^{adaptive}\right| = \frac{\left[\left(v_\alpha - Ri_\alpha\right)^2 + \left(v_\beta - Ri_\beta\right)^2\right]^{1/2}}{\sqrt{3/2}\lambda_m + \Delta} \ . \tag{109}$$

A block diagram of the proposed adaptive velocity correction technique based on (109) is shown in Fig. 14. Initially, the PM flux linkage error term Δ is set to zero. However, as long as the magnitude of the estimated velocity is above the low speed threshold (stable rotor angle estimation), the adaptive velocity estimation process is activated. The adaptive velocity estimation process compares the estimated rotor velocity with $d\hat{\theta}/dt$ to generate a velocity estimation error signal. A PI controller operates on this estimation error - adjusting the output Δ to .

The time constant of the PI controller using in Fig. 14 is chosen to be slow, since the temperature effect that causes drift in the permanent magnet flux linkage parameter is a very slow effect as well. This has the benefit that the noise generated by the differentiation of the rotor angle estimate is smoothed over time. Thus, as long as the rotor position estimator remains stable (synchronous operation), the average value of its derivative is equal to the actual rotor speed.
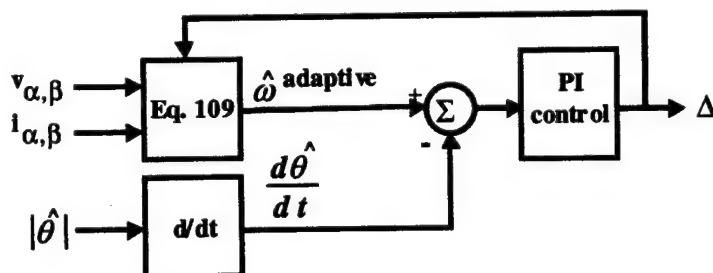

Fig. 14 Adaptive velocity estimation block diagram

An experiment showing the adaptive velocity feedback strategy performance was conducted where the sensorless drive was operating in the current control mode. For this experiment, the permanent magnet flux linkage term of the internal model was intentionally set to a value 20 percent greater than its nominal value of 0.166 v-s. With this error in the flux linkage constant, the estimated rotor velocity from (69) will be lower in magnitude than the actual velocity. Fig. 15 shows how the adaptive velocity estimation scheme corrects the PM flux linkage constant such that the estimated velocity converges toward the actual velocity measured with an encoder. In this experiment, the adaptive velocity estimator is activated at zero seconds and converges toward the actual velocity despite the initial error in the parameter. In the figure, the error in the PM flux linkage constant Δ is also shown to converge to a value of 0.029 v-s, which is the error intentionally introduced in this parameter. From this view, this strategy may be used for parameter estimation of the PM flux linkage constant λ_m. It should be noted that in this test, the adaptive velocity is not used as an input to the position estimator.
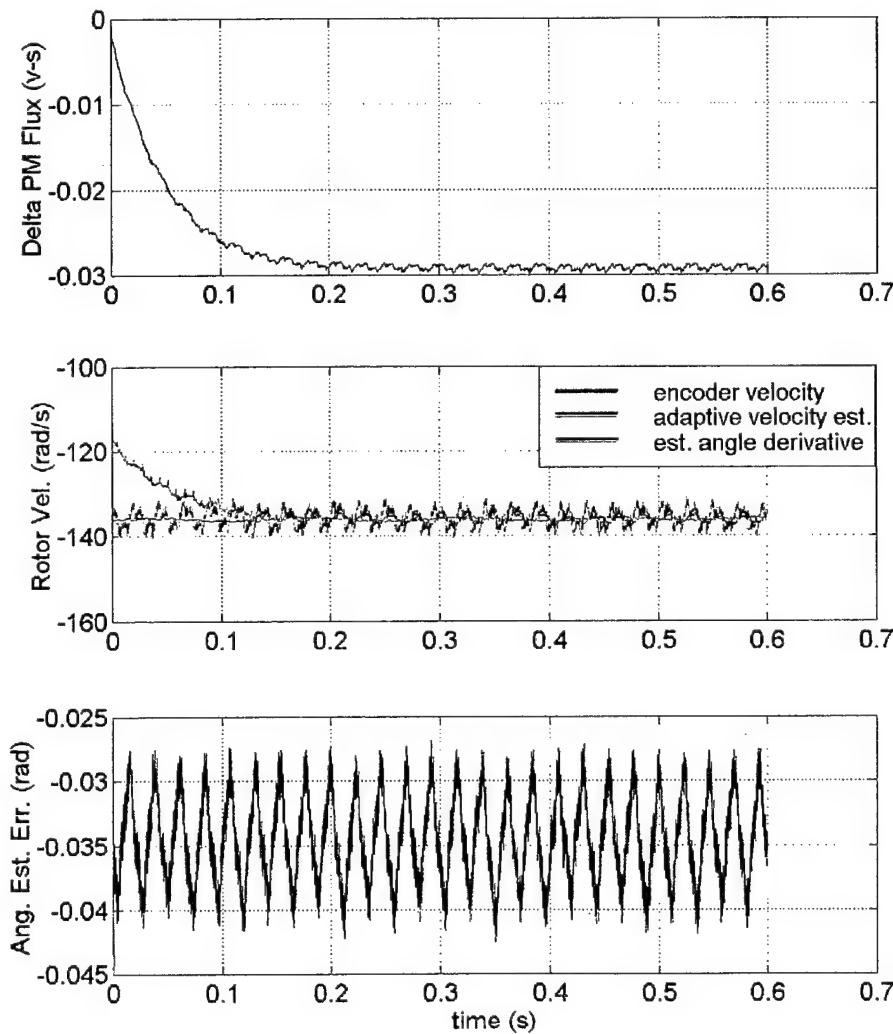
Fig. 15 Adaptive velocity estimation with parameter uncertainty in PM flux linkage constant

5   SENSORLESS PMSM EXPERIMENTAL RESULTS

In this chapter, experiments on the developed sensorless drive are carried out. All of the experiments are executed using the developed sensorless drive hardware, which controls the PMSM in real-time using the estimated rotor angle and speed.   The results demonstrate the effectiveness of the proposed control method for a wide variety of operating contitions.

5.1   Experimental System

To evaluate the performance of the sensorless drive, a set of experiments were performed where the rotor position observer executes the rotor position estimation algorithm in real-time. The estimated rotor angle is provided to the current controller described in section 4.2.1. The test setup used in the experiments is shown in Fig. 16.
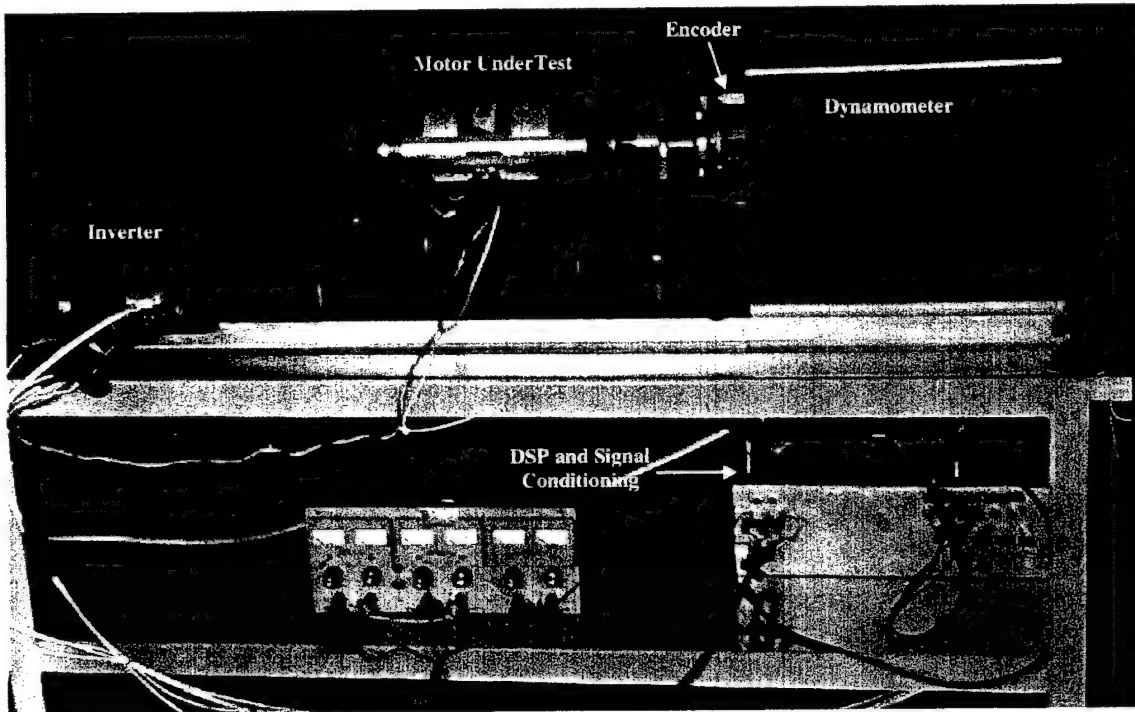
Fig. 16 Experimental setup for sensorless drive

The mechanical arrangement consists of a PMSM whose shaft is coupled directly to a magnetic particle dynamometer, as shown in the figure. To allow rotor position observer accuracy to be determined, a hollow shaft encoder was attached to the shaft at the dynamometer base. Two easily interchangeable test motors were used for experimental testing of the sensorless drive – both a slotless (shown in Fig. 17) and a slotted machine (Fig. 18). The parameters for the machines used in the experiments are given in Tables 1 and 2.

Table 1. Parameters of slotless motor - Electric Indicator Company model 4440PSKX-3788

Per Phase Resistance	1.35 Ω
Per Phase Inductance	.131 mH
Permanent Magnet Flux Linkage	.115 v-s
Rated Power	2.5 HP
Poles	8

Table 2. Parameters of slotted motor – Custom Servo Motors model MPM1422A

Per Phase Resistance	.12 Ω
Per Phase Inductance	1.1 mH
Permanent Magnet Flux Linkage	.166 v-s
Rated Power	6.8 HP
Poles	6
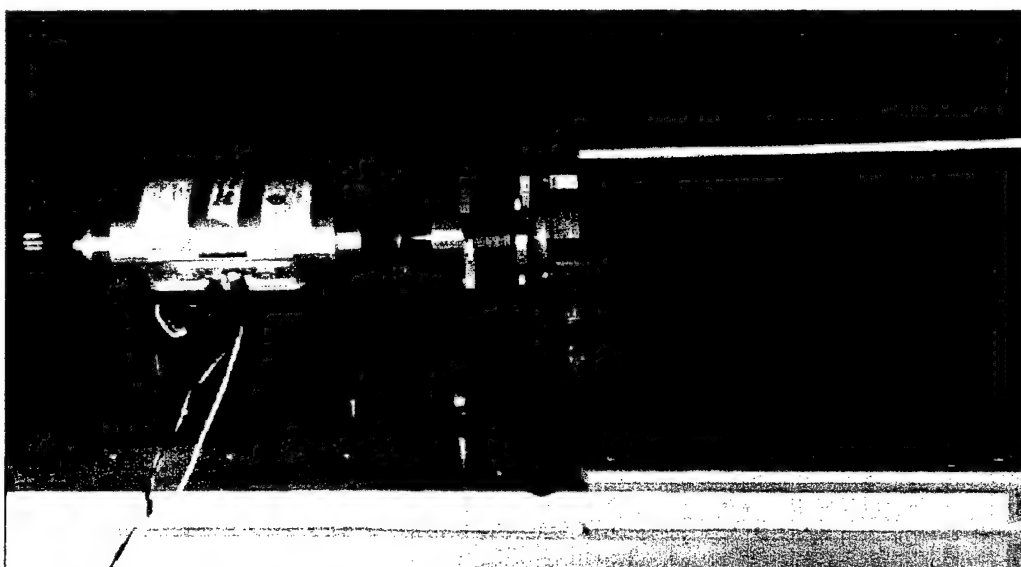
Fig. 17 Mechanical configuration of sensorless testbed
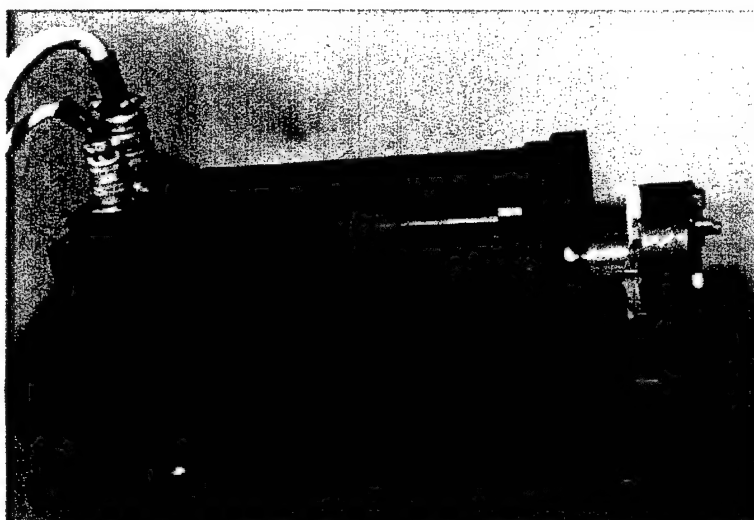
Fig. 18 Custom Servo Motors slotted PMSM used for sensorless drive development

The architecture for the implementation of the prototype sensorless electric drive consists of a floating point digital signal processor (DSP), a fixed point motor control DSP, and a personal computer (PC). A block diagram of the system is shown in Fig. 19. The personal computer acts as the host for the ISA bus-based floating point DSP board, providing a graphical user interface for operating the drive, displaying the drive performance status, and storing relevant operational data. The floating point DSP (Bittware model SNAG-4060-112) performs the rotor position and velocity estimation at 100 μs and 2 ms intervals, respectively. In velocity control mode, the floating point DSP executes the velocity control algorithm described in section 4.2.2. The fixed point motor control DSP (Analog Devices ADMC301) is used to sample the stator voltages and currents, provide the deadtime compensated PWM signals to the inverter (Servo Dynamics Model SDBDTL 1-1525-17-1 and Copley Controls Model 7429AC), and implement the current control scheme described in section 4.2.1. The PWM frequency for the sensorless drive is 22 kHz.

The two DSPs communicate directly via a high speed (8 Mbaud) serial link. This link allows the two processors to share the required data. The floating point DSP sends the rotor angle estimate and current commands to the motor control DSP, while the motor control DSP transmits the measured currents and voltages back to the floating point DSP. Although the high speed serial link was adequate for the prototype sensorless drive, it is recommended that in any future implementations the DSPs either become more tightly coupled (sharing common memory or data bus) or all software be ported to a single processor.
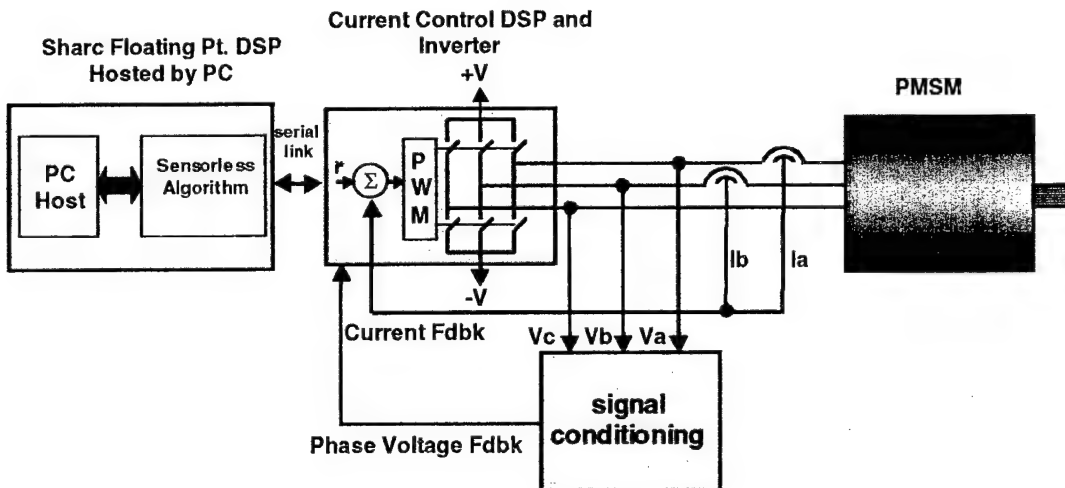

Fig. 19. Block diagram of experimental system

5.2 Experimental Results

Using the sensorless PMSM drive setup described in the previous section, the rotor position estimation accuracy was evaluated for various steady state and transient operating conditions. In addition, the effects of sensorless operation on operating efficiency and radiated noise were examined by comparing the performance of the

proposed sensorless drive with a drive using a high resolution rotor position sensor. Comparisons are also made to a drive utilizing discrete Hall effect rotor position sensors since these devices are often used to commutate the PMSM where an encoder or resolver cannot be tolerated [24].

5.3 Rotor Position Estimation Accuracy

In order to evaluate the rotor position estimation accuracy, a high resolution encoder was attached to the shaft of the PMSM under test. The encoder was used only as a reference for evaluating the accuracy of the estimated rotor position. That is, the estimated rotor position was used to commutate the PMSM. In the following, the steady state and transient rotor position estimation accuracy is evaluated for both the slotted and slotless test motors under various operating conditions.

5.3.1 Steady State Rotor Position Estimation Accuracy

Figs. 20 and 21 show the rotor position estimation error for various speeds on the slotless and slotted PMSM, respectively. For these tests, the phase voltages are measured directly using the methods of section 4.1.1.2. Although the performance of the rotor position is excellent, the required low-pass filtering of the phase voltage results in an estimation error that increases with rotor speed (frequency). This degradation in rotor position estimation as speed increases is due to the phase shift introduced by low-pass filtering the phase voltages. In order to remove the PWM switching from the voltage signals, a linear active, 4 pole, 5 kHz butterworth filter (Frequency Devices Model D74L4-5KHz) was used. The use of the filter results in a delay of 80 µs, or a phase shift that is linearly dependent on frequency. This linear phase shift corresponds to 3 electrical degrees for 100 Hz, where 100 Hz is 1500 and 2000 RPM for the slotless and slotted motors, respectively. The effect of the low-pass filter is clearly seen in Figs. 20 and 21, where the estimation error is increasing linearly with speed (frequency).

The experiment shown in Fig. 21 is now repeated using the indirect voltage reference strategy described in section 4.1.1.1 used to obtain the phase voltage. The results are shown in Fig. 22. Using this strategy, the effects of the low pass filter are removed, and steady-state angle estimation is significantly improved through the higher speed range when compared with the direct phase voltage measurement technique of Fig. 21. However, the performance of the voltage reference method is not as accurate as the direct voltage measurement technique in the low-speed range. These results suggest the possibility of using a changeover from direct phase voltage measurement to the indirect voltage reference method at some threshold rotor speed.

In Fig. 23 a direct and indirect measurement of phase voltage are compared at an angular velocity of 1000 RPM. The delay of the directly measured quantity due to the low pass filter is evident in this figure.
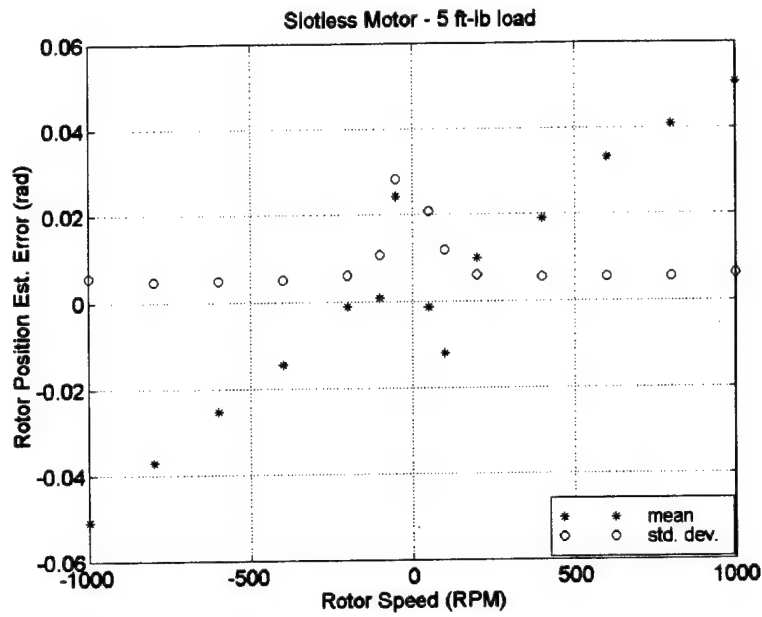
Fig. 20 Rotor position estimation accuracy of slotless PMSM using direct phase voltage measurement
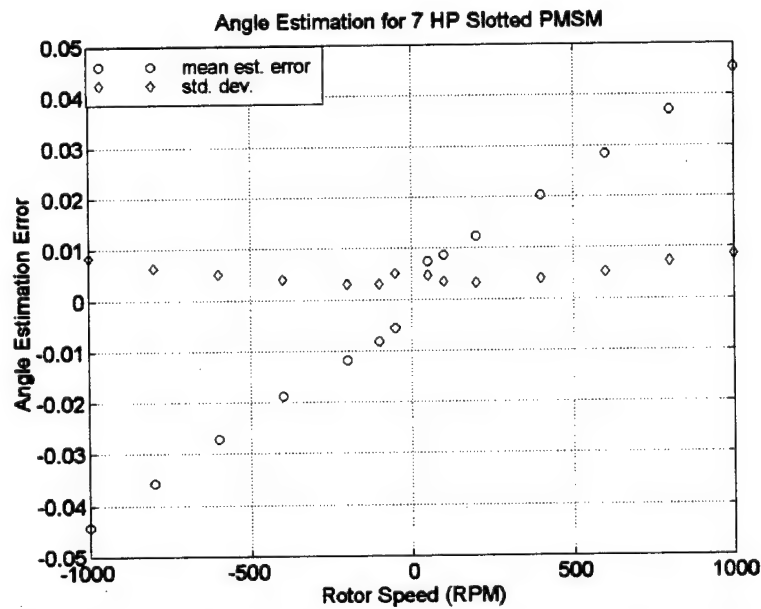

Fig. 21 Rotor position estimation accuracy of slotted PMSM using direct phase voltage measurement

The degradation in low speed performance when using the indirect phase voltage measurement method may be explained by considering that for high speeds, the commanded voltage v^* is large with respect to any output voltage errors and the ratio $\Delta v/v^*$ becomes negligible. The term Δv represents the output voltage error (i.e. the difference between the voltage command reference and the actual phase voltage). At lower speeds, however, v^* is small and even small errors in the voltage due to modeling inaccuracies associated with the inverter components will yield relatively large errors in

43

estimating the phase voltage. That is, phase voltage errors become negligible at high speed, but significant at low speed. It should be noted that in general, the voltage drops of the switch and diode (v_d and v_t in eqs. 82-83) increase with the current level. Although this effect has not been accounted for in the analysis of section 4.1.1.1, its inclusion is straightforward and would improve the performance of rotor estimation at low speeds when using the voltage reference as the phase voltage measurement.
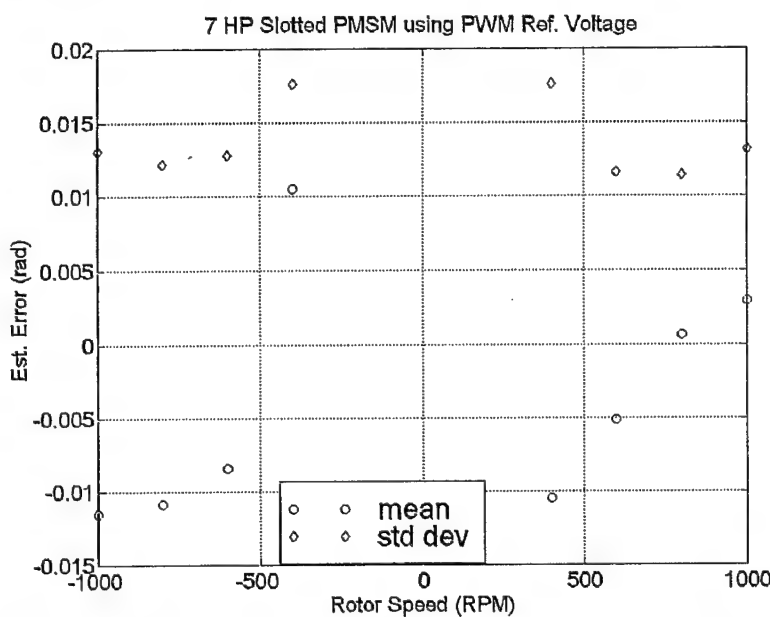
Fig. 22 Rotor position estimation accuracy of slotted PMSM using reference voltage
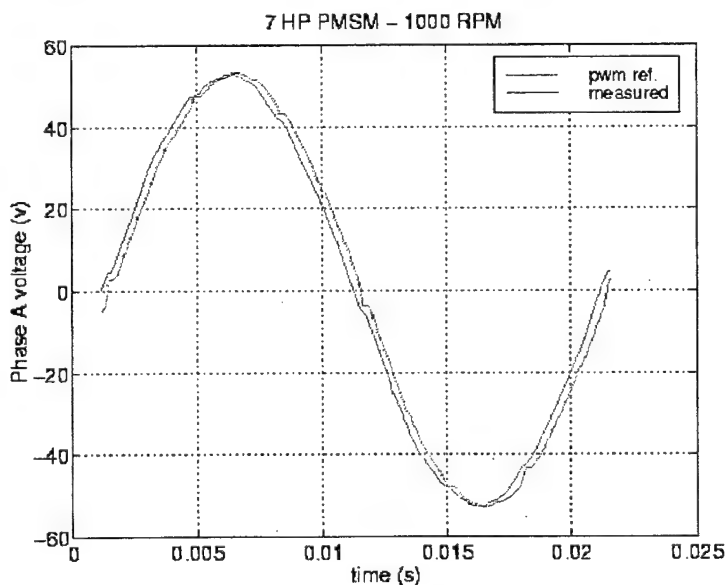
Fig. 23 Comparison of reference voltage and measured phase voltage at high speed

44

In Fig. 24, the steady-state rotor position estimation accuracy is compared for various observer pole scheduling designs. For this experiment, the pole locations are scheduled based on the rotor speed such that the observer pole location is approximately n times faster than the angular speed, where n is 3, 12, and 18, for the three cases shown in the figure. The observer pole locations indicated in the figure correspond to the scheduled location of the observer poles at 100 RPM.
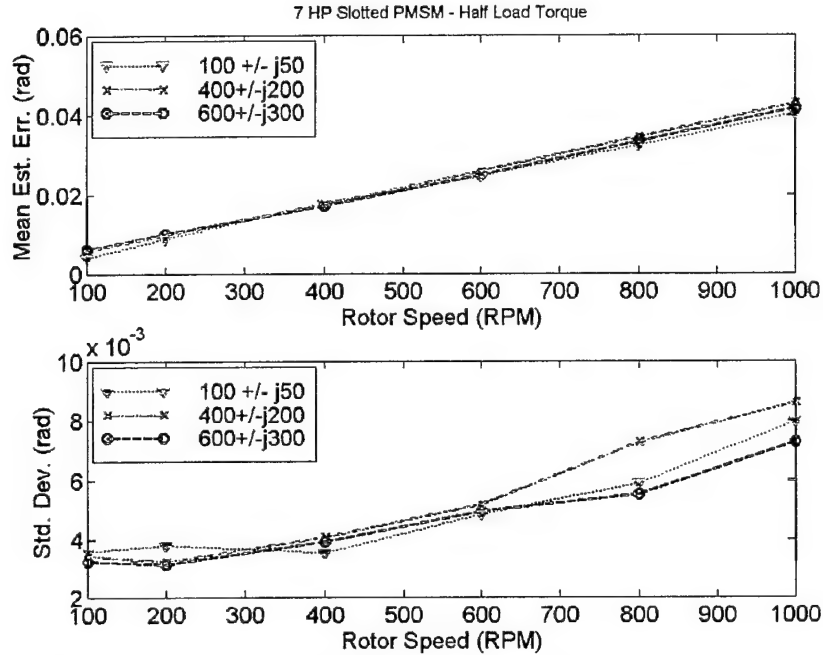
Fig. 24 Rotor angle estimation in steady state for various observer gain schedules

It is clear in Fig. 24 that the pole location has no significant effect on the steady-state rotor position estimation. This may be explained with the help of the error dynamics given by (73). The solution to the error dynamics is

$$\mathbf{e}(t) = \phi(t)\mathbf{e}(0) \tag{110}$$

for $t \geq 0$ and the state transition matrix ϕ is given by

$$\phi(t) = \mathcal{L}^{-1}\left\{(s\mathbf{I} - \mathbf{A} + \mathbf{GC})^{-1}\right\}. \tag{111}$$

Thus, if the eigenvalues of $[\mathbf{A} - \mathbf{GC}]$ are in the left hand complex plane, asymptotic state reconstruction occurs and the error vector approaches zero as $t \rightarrow \infty$. It is the pole placement strategy that maintains the eigenvalues in the LHP. Although this result indicates zero steady state estimation error, in practice it is generally difficult to achieve this due to the presence of infidelities in the observer input signals.

As discussed in section 3.2.2, operation of the sensorless drive at extremely low speed is problematic because the rotor angle is not an observable quantity under those conditions. At such low speed, the rotor position feedback should be disabled. Selection of the low speed threshold was performed experimentally, and was set to 10 rad/sec (approximately 23 RPM for an 8 pole PMSM) for the prototype sensorless drive. In Fig. 25, the operation of the 8 pole PMSM at 30 RPM is shown.
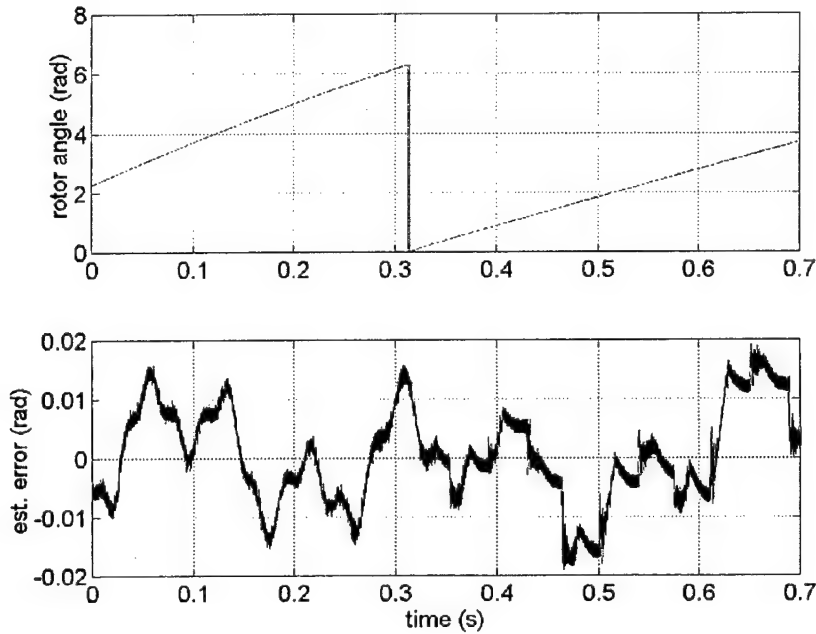

Fig. 25 Performance of rotor position estimator at very low speed for slotted PMSM

5.3.2   Transient Rotor Position Estimation Accuracy

The observer poles are selected to satisfy the system requirements of rapid response and stable estimation of the rotor position. If poles are placed too far into the left hand plane, then the rate of convergence is increased, but observer stability will be diminished. In practice, it was found that if the observer poles remain relatively slow in comparison to any anti-aliasing filters and faster than the system poles, good performance is achieved. In the implementation, the poles are scheduled according to the estimated velocity such that the observer poles are at least 5 times faster than the system poles. Fig. 26 shows the response of the error dynamics with an initial angle estimation error of 10 electrical degrees for several observer pole locations. The slotless PMSM is operating at 100 RPM (approximately 50 radian/s) for this test.

During a speed reversal, the rotor velocity passes through the problematic zero speed range. While the magnitude of rotor velocity is below the low speed threshold, the rotor position observer operates without feedback. Such operation has been shown through experimentation to be acceptable for short time intervals, such as during a speed reversal. In Fig. 27, the rotor position observer is examined during a speed reversal. In the figure,

the estimated velocity magnitude drops below the threshold at 0.35 sec. and the observer operates without feedback until 0.48 seconds, where feedback is restored. From the estimated states in the figure (flux linkage and trigonometric functions of the rotor angle) it is seen that the open loop observer structure produces excellent results, or ride-through capability for short term operation below the low speed threshold.
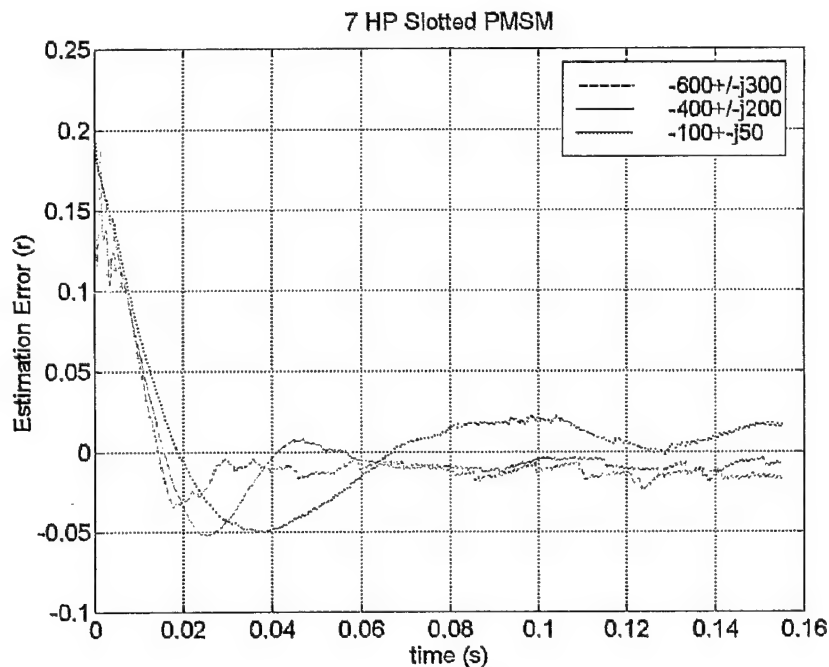

Fig. 26 Transient response of rotor position estimator with various observer pole locations
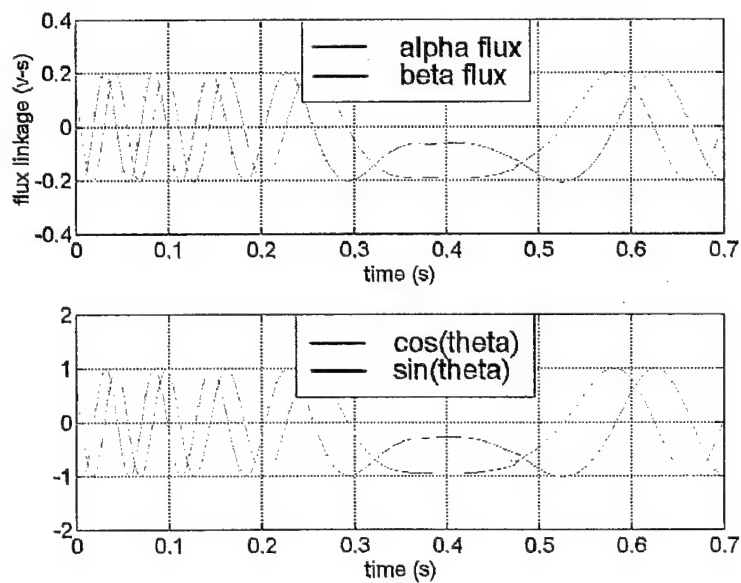
Fig. 27a Sensorless PMSM estimated state variables during speed reversal

47
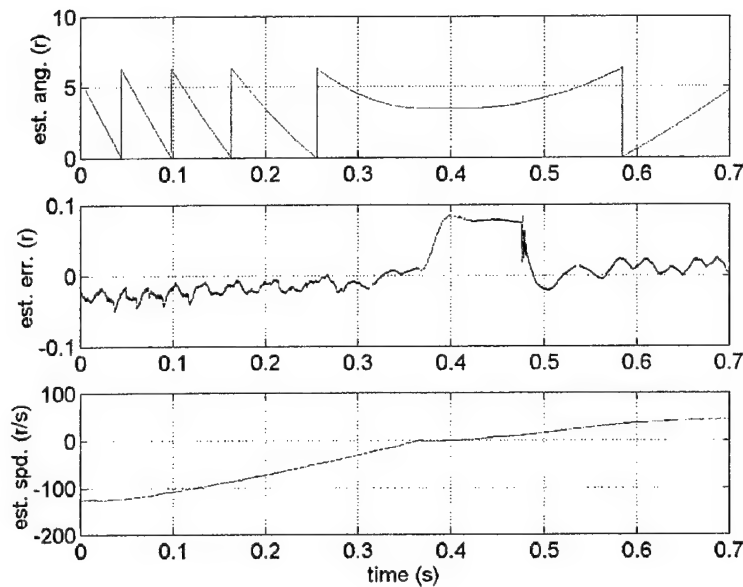
Fig. 27b Sensorless PMSM rotor angle and speed estimation during speed reversal

Although the open-loop model produces good results for short term operation at very low speed, it will not be adequate for initial startup from zero speed. In the absence of a suitable zero speed rotor position detection method[*] or coarse Hall effect position sensors, an asynchronous starting strategy must be employed to ramp the PMSM to the low speed threshold, at which time the estimated rotor position assumes synchronous operation of the machine. A startup of the sensorless PMSM is shown in Fig. 28, where the rotor speed reaches the low speed threshold at 0.36 seconds. At this time, the rotor position observer is activated (with feedback) and the estimation error quickly converges toward zero.

The PMSM model (62-65) used to construct the rotor position observer does not include mechanical parameters such as friction, inertia, and load torque. Thus, the rotor position observer is expected to be independent of the load torque and other mechanical parameters. In Fig. 29, a fast load change is applied to the slotted PMSM while operating at a speed of 400 RPM. As expected, the estimation accuracy is not effected by this disturbance.

---

[*] The author has submitted PSU Invention Disclosure No. 99-0692 "*Detection of Rotor Angle in a Permanent Magnet Synchronous Motor at Zero Speed*" to provide rotor position at startup
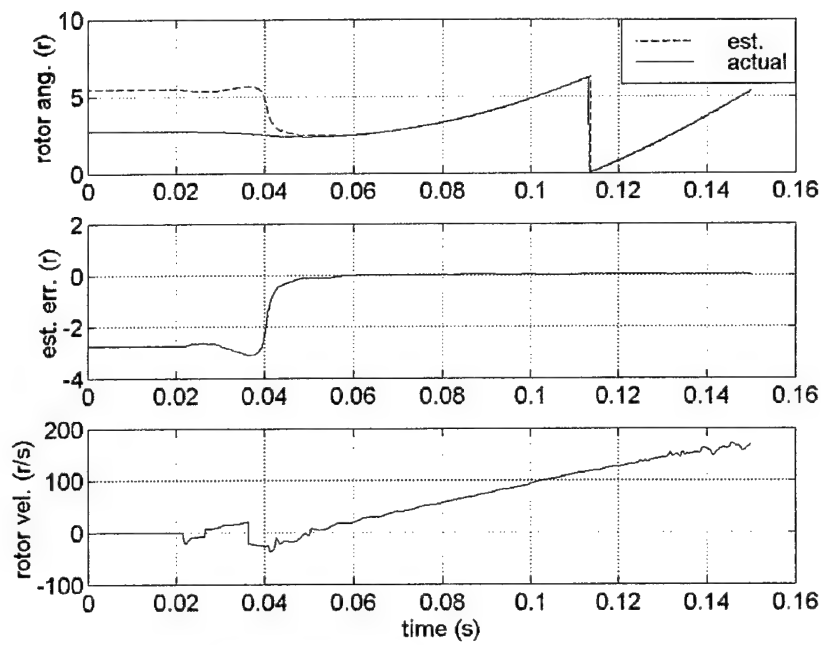
Fig. 28 Rotor position estimation from startup from zero speed
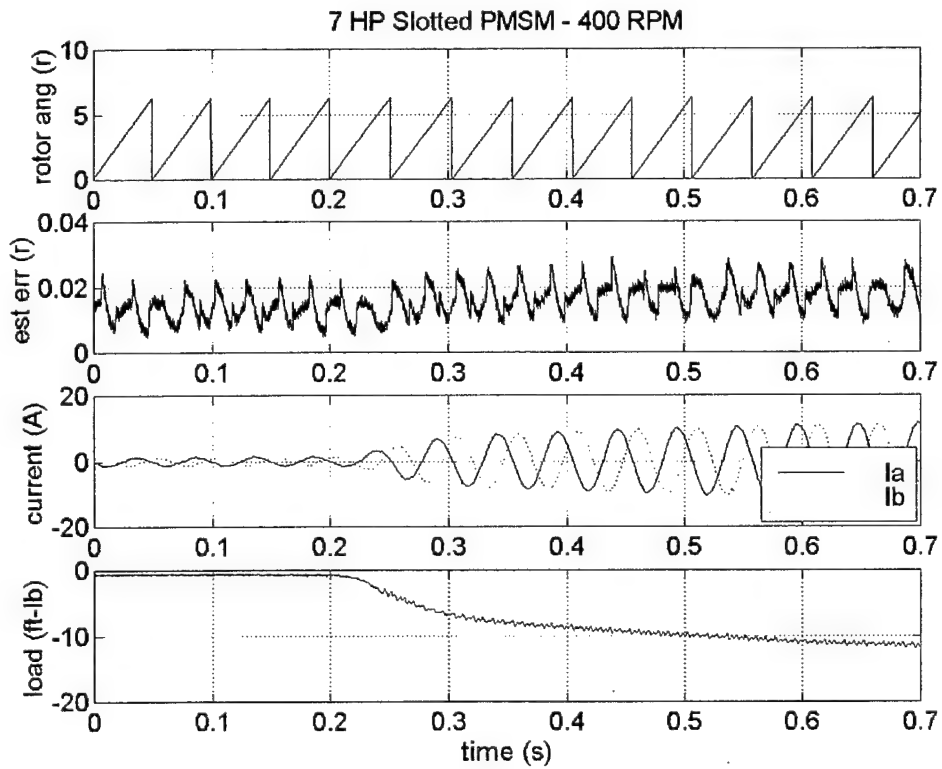
Fig. 29 Sensorless PMSM performance during a sudden load torque change

49

5.3.3 Rotor Position Estimation Robustness

In this section, the robustness of the developed sensorless PMSM drive is examined with respect to parameter uncertainty and external disturbances. In practical applications, machine parameters vary due to temperature effects. Therefore, an effective rotor position estimator must be robust to these errors in the machine model.

In the PMSM, the machine parameters λ_m and R may vary inversely and proportionally with the temperature, respectively. To determine the effect these parameter variations have on the rotor position estimation process, these internal model parameters are intentionally detuned by 20 percent in various combinations while the rotor angle estimation accuracy is measured. The tests were performed using the slotted PMSM at a load torque of 5 ft.-lb. and angular velocity of 400 RPM. The results shown in Figs. 30 and 31 demonstrate robustness to these parameter variations – especially the stator resistance. In these figures, the PM flux linkage λ_m is designated by the symbol K_e. The estimation accuracy dependence on PM flux linkage is primarily due to the errors this parameter has on the estimated angular velocity. Although a method for correcting the PM flux linkage parameter error has been examined in section 4.2.2, it is not used for the tests described in this section since the intent was to examine the effects of such errors.

The effect of load torque disturbances is shown in Fig. 32. For the reasons discussed in the previous section, load torque is seen to have virtually no effect on rotor position estimation accuracy.
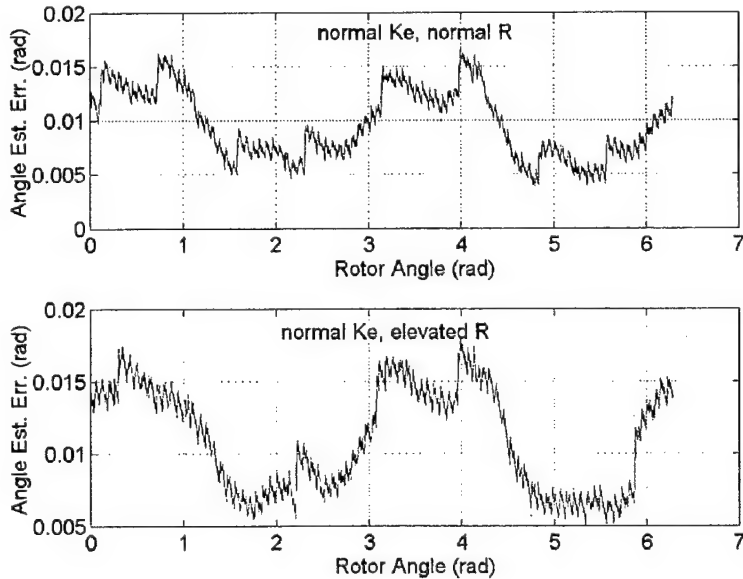

Fig. 30 Rotor angle estimation accuracy with respect to stator resistance uncertainty
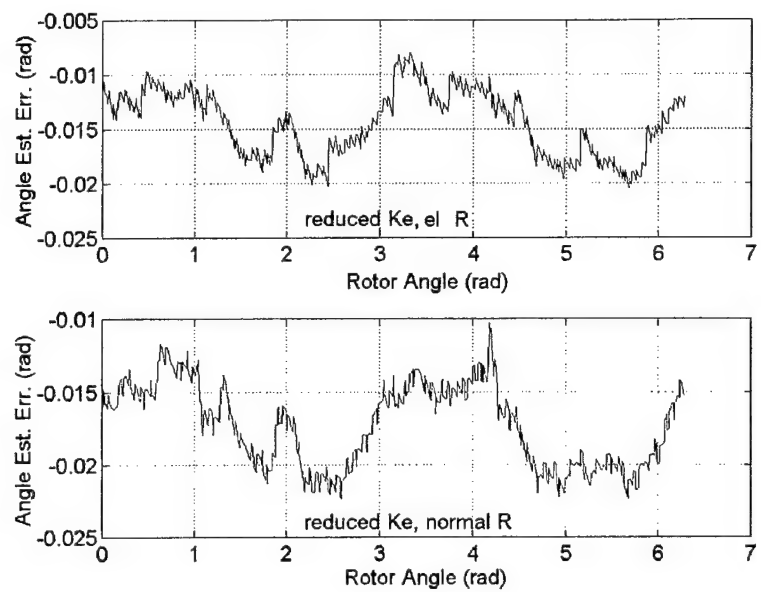
Fig. 31 Rotor angle estimation accuracy with respect to PM flux linkage and stator resistance uncertainty
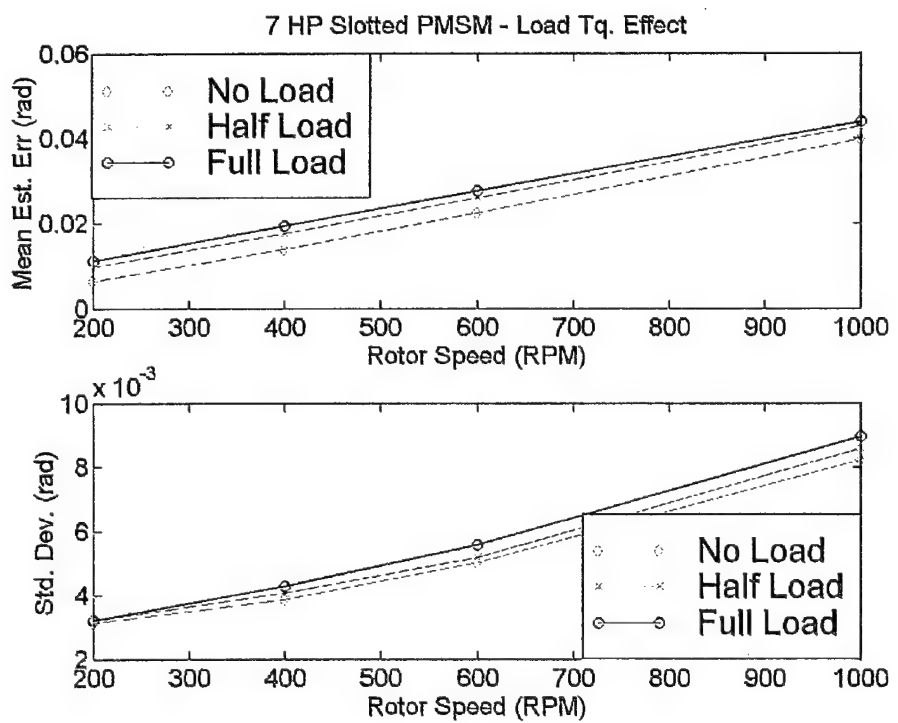

Fig. 32 Rotor angle estimation accuracy with respect to load torque disturbances

5.4 Motor Efficiency

Permanent magnet machines can offer significant efficiency advantages over the induction and DC machine when employed in adjustable speed drives. The PM motor operates at synchronous speed and does not have the slip losses inherent in induction machines. In addition, the PM machine does not have losses associated with the magnetizing component of stator current. It also does not suffer from the losses or limitations associated with the brushes in a DC machine.

To determine the effect of sensorless operation on operating efficiency in the PMSM, an experiment in which rated load is applied to the shaft of the slotless machine was performed. In this test, three rotor position feedback modes are used to commutate the PMSM while the operating efficiency is measured – coarse Hall sensor, high-resolution encoder, and the proposed sensorless method. In the case of the Hall sensor feedback mode, the average torque angle was maintained at 90 electrical degrees. For both sensorless and encoder feedback modes, the torque angle was maintained at 90 electrical degrees, giving maximum torque per unit current. The results of this test are shown in Fig. 33, and indicate a significant difference between the sinusoidal current control (provided by the sensorless and encoder modes) and trapezoidal control provided by the Hall sensor mode. There is no measurable difference in operating efficiency between sensorless and encoder feedback control for rotor speeds above the low speed threshold.
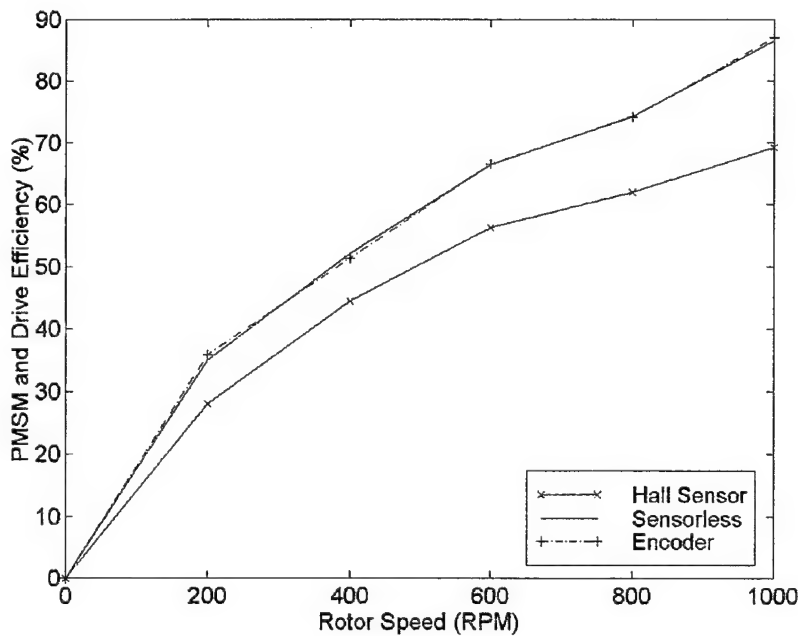

Fig. 33 Efficiency of slotless PMSM at full load with various commutation strategies

5.5 Acoustic Performance

In order to determine the effect of the sensorless drive on acoustic performance, measurements of prototype sensorless drive with slotless motor were taken in an anechoic chamber. Figs. 34 and 35 shows the test assembly and instrumentation configuration for these tests. The prototype drive was set up such that three rotor position feedback modes may be used: Hall sensor, sensorless, and rotary encoder (8000 line). Measurements of the radial acceleration and airborne noise were taken at various operating conditions for each of the three rotor position feedback modes. The results are included in Figs. 36-46.
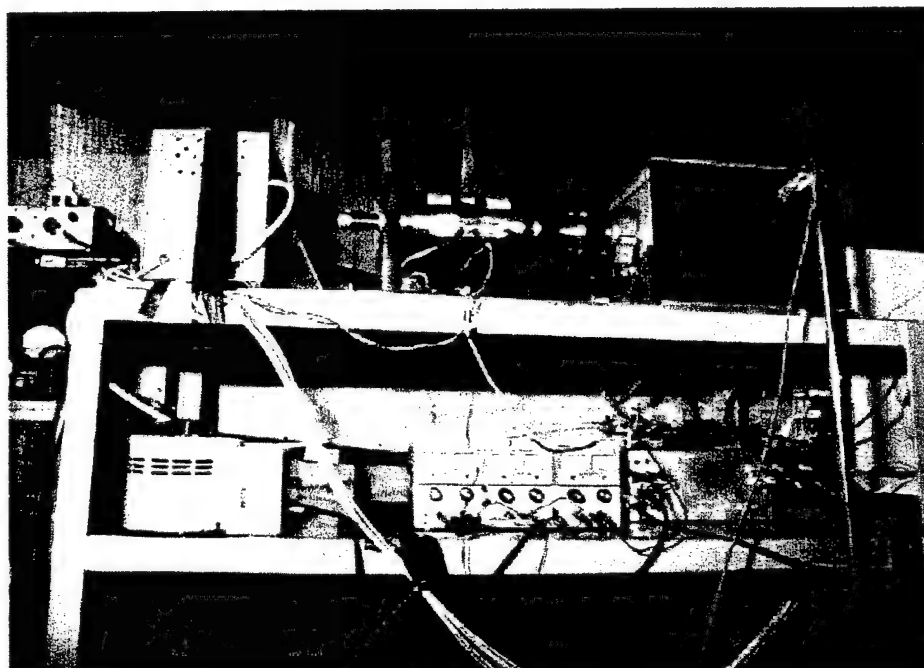
Fig. 34 Sensorless PMSM anechoic chamber test setup
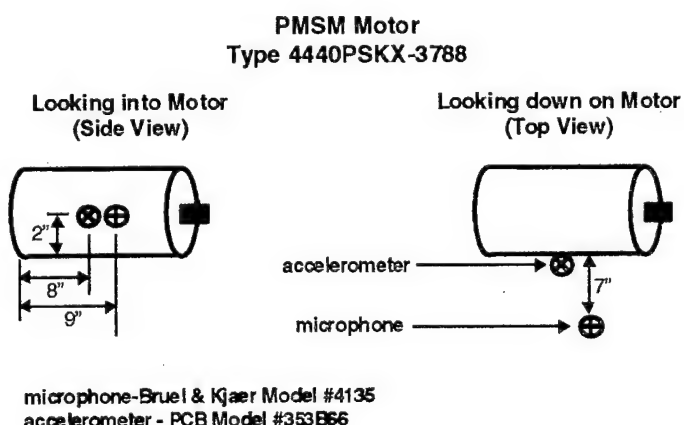
Fig. 35 Instrumentation and location for anechoic chamber testing of sensorless PMSM

53

In Figs. 36-39 and 40-43, the radial acceleration and measured airborne noise for each of the three commutation modes is shown for low (6.6 Hz) and medium (40 Hz) rotor speed, respectively. For these tests, the slotless PMSM is operated at half the rated load torque. The use of high resolution rotor position information in the encoder and sensorless modes result in decreased radiated noise when compared to the Hall sensor mode. There is no significant difference in the radiated noise between sensorless and encoder modes of operation, as demonstrated in Figs. 38,39 and 42,43. High speed comparison between sensorless and encoder position feedback modes is shown in Fig. 44.
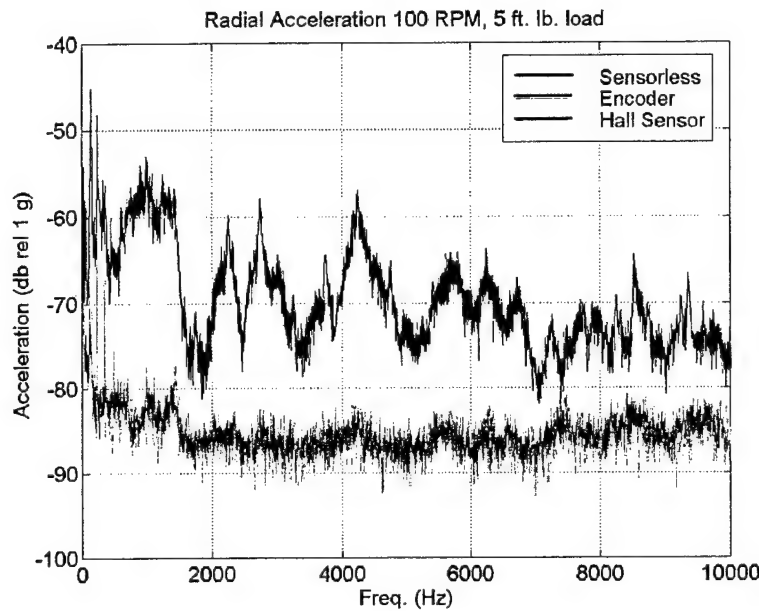

Fig. 36 Radial acceleration of slotless PMSM for various position feedback sources
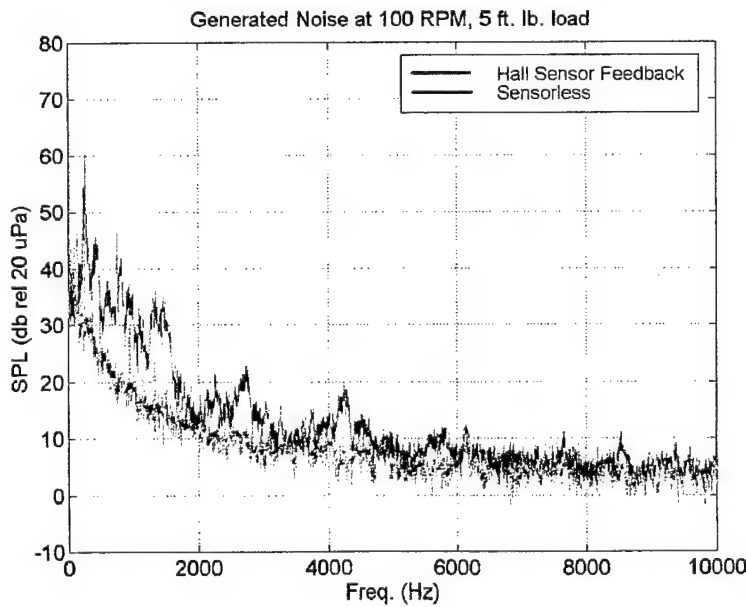
Fig. 37 Generated noise comparison for coarse position feedback and sensorless operation

54
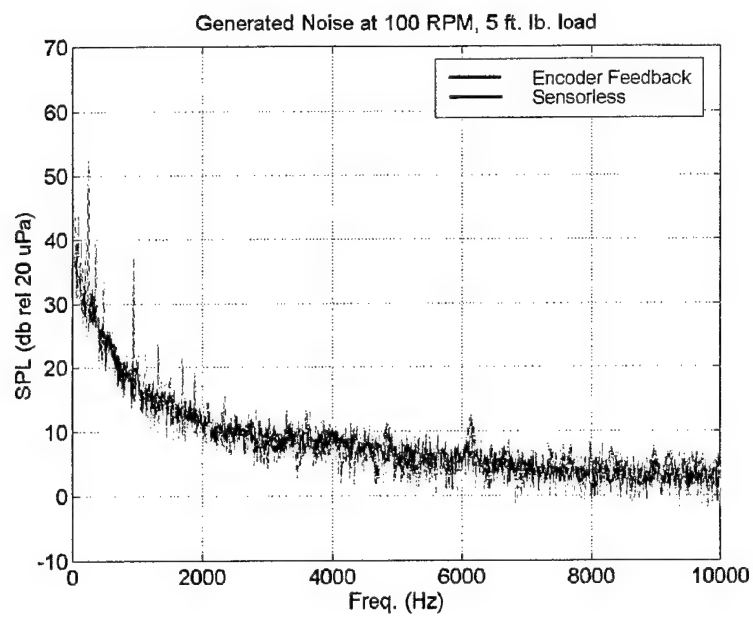
Fig. 38 Generated noise comparison for encoder position feedback and sensorless operation
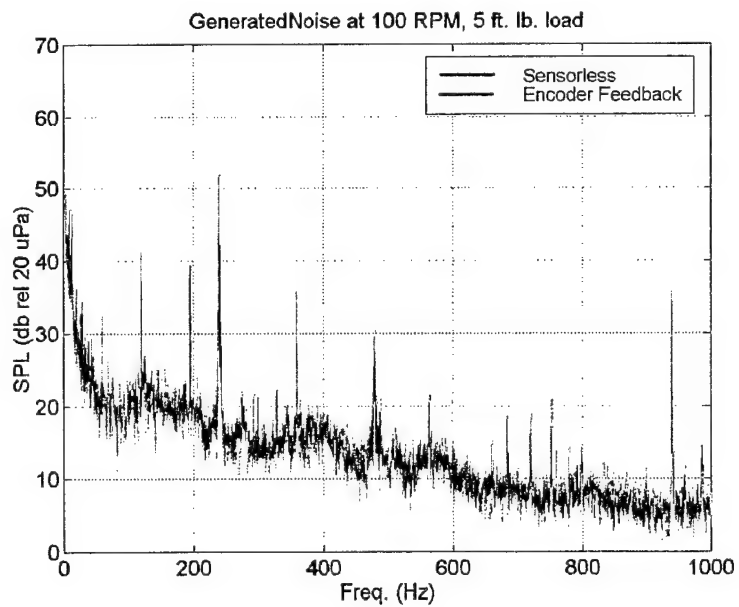

Fig. 39 Generated noise comparison for encoder position feedback and sensorless operation
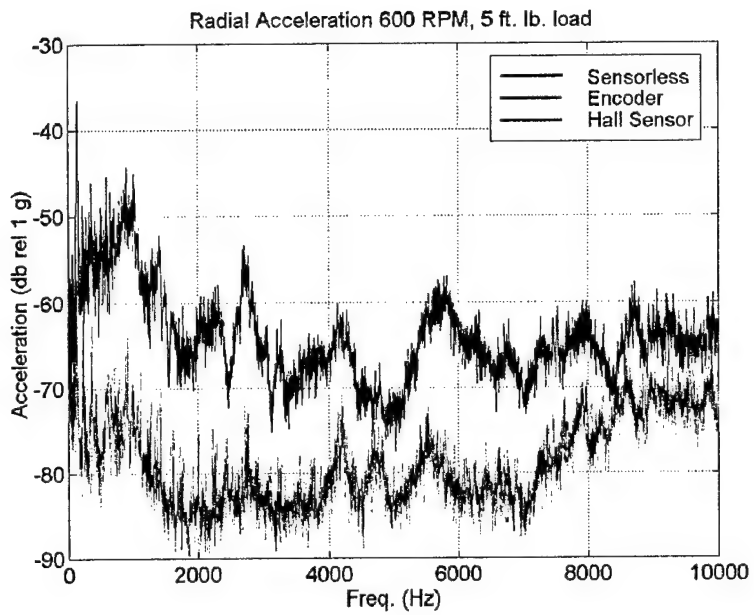
Fig. 40 Radial acceleration of slotless PMSM for various position feedback sources
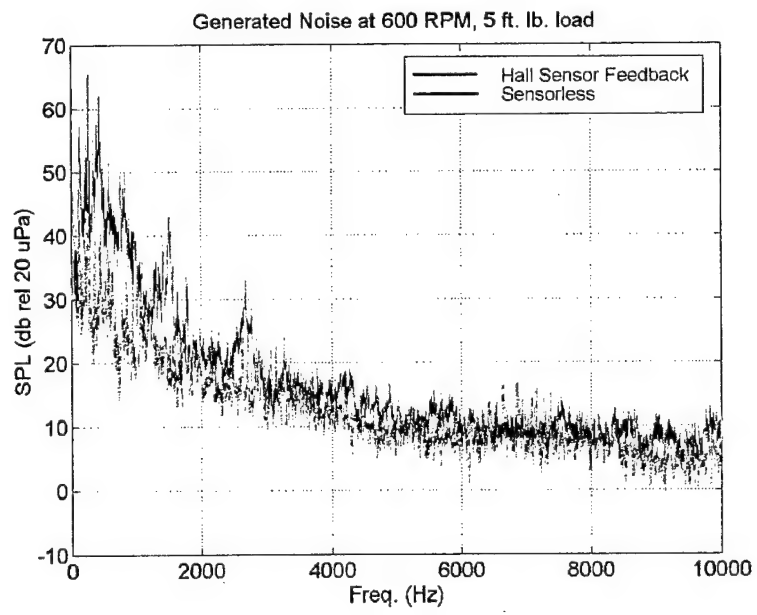

Fig. 41 Generated noise comparison for coarse position feedback and sensorless operation
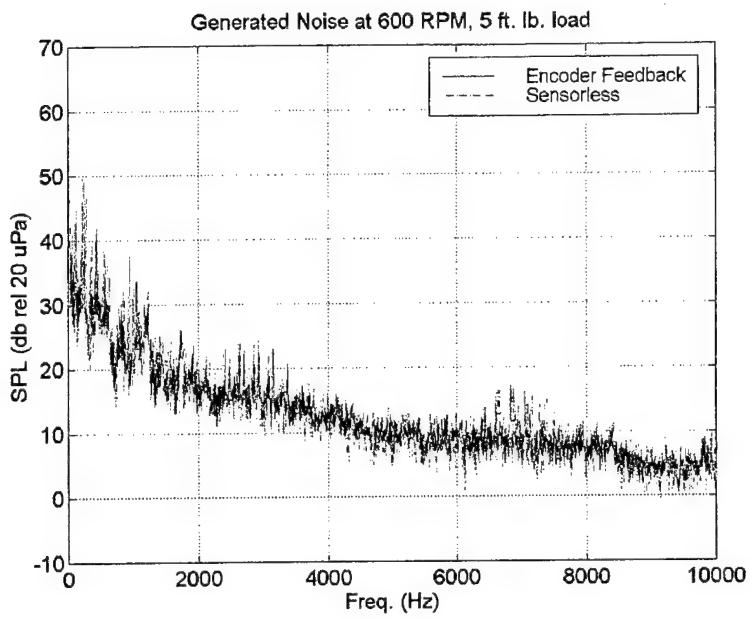
Fig. 42 Generated noise comparison for encoder position feedback and sensorless operation
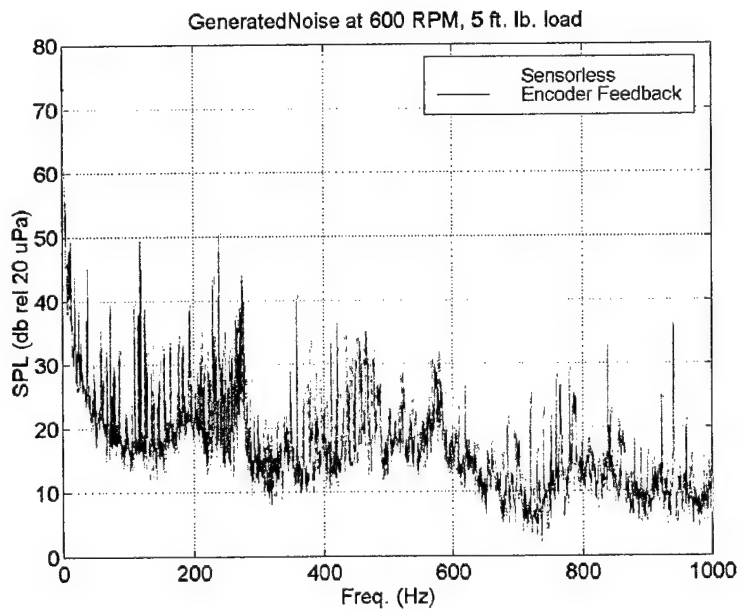
Fig. 43 Generated noise comparison for encoder position feedback and sensorless operation
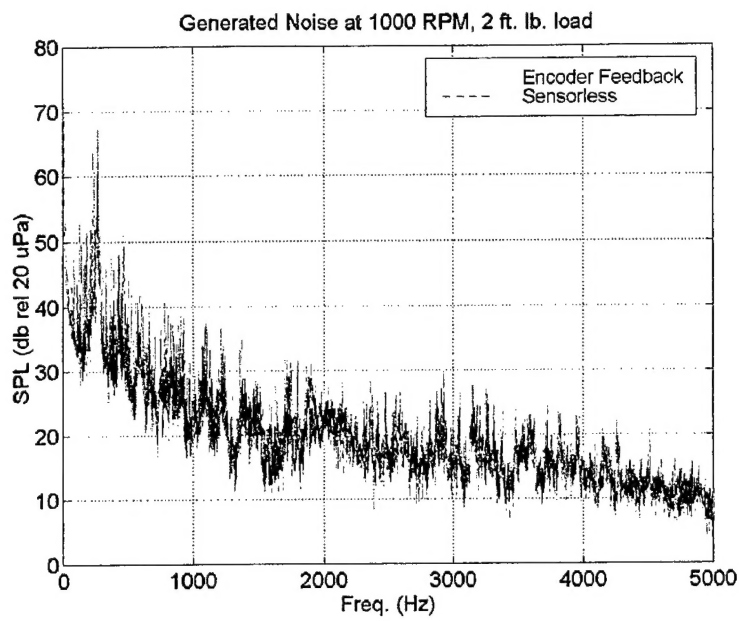
Fig. 44 Generated noise comparison for encoder position feedback and sensorless operation at high speed

6   CONCLUSIONS

This document describes in detail the design and implementation of a rotor position sensorless electric drive for a permanent magnet synchronous motor (PMSM). The paper further illustrates some experimental studies that were conducted on the prototype sensorless drive. These studies include steady state and transient estimation accuracy, robustness, disturbance rejection, efficiency, and acoustic performance. Through experimentation, the proposed sensorless drive is shown to be extremely accurate and robust to parameter uncertainty and disturbance. In terms of conversion efficiency and acoustic emission, the experimental results demonstrate that sensorless PMSM delivers performance comparable to sensor based PMSM control – except for operation around zero speed. It has been demonstrated that the reduced dependability and added complexity, cost, size, and weight of the mechanical sensor provides only a limited increase in performance over the proposed sensorless strategy, with clear advantages of sensor based control only evident around zero speed. Therefore, the results of this study suggest that the developed sensorless strategy is a viable alternative for many Navy drive applications requiring the high power density, efficiency, and reliability of the sensorless PMSM combination. The sensorless drive design, experimental results and implementation issues addressed in this study will serve as valuable information for any future sensorless drive design endeavors.

7 ACKNOWLEDGEMENTS

The following personnel offered valuable assistance and feedback during the course of this project:

Tom Calvert, NUWC Carderock
Lynn Petersen, NUWC Carderock
Gordon McKibbon, NUWC Carderock
David Bagley, Vector Research
Mark Turner, Applied Research Laboratory
Joseph Welz, Applied Research Laboratory
Rick Marboe, Applied Research Laboratory
Edward Boone, Applied Research Laboratory
Dr. K.Y. Lee, Pennsylvania State University Dept. of Electrical Eng.
Daniel Thivierge, NUWC Newport

8 REFERENCES

[1] F. Salberta, J. Mayer, R. Cooley, *"An improved control strategy for a 50 kHz auxiliary resonant commutated pole converter"*, Power Electronics Specialists Conference (PESC) v. 2, June 1997, pp. 1246-1256.

[2] J. Lai, *"Resonant snubber based soft-switching inverters for electric propulsion drives"*, IECON, v. 1, 1996, pp. 47-52.

[3] W. Shireen, C. Andrews, J. Chepin, *"A MCT based zero voltage switching PWM inverter"*, Applied Power Electronics Conference and Exposition, vol. 2, 1997, pp. 770-775.

[4] S. Chung, H. Kim, C. Kim, M. Youn, *"A new instantaneous torque control of permanent magnet synchronous motor for high performance direct drive applications"*, Applied Power Electronics Conference and Exposition, 1997, v. 2, pp. 721-727.

[5] L. Zhong, M. Rahman, W. Hu, K.Lim, *"Analysis of direct torque control in permanent magnet synchronous motor drives"*, IEEE Transactions on Power Electronics, v. 12, no. 3, May 1997, pp. 528-536.

[6] S. Morimoto,Y. Tong, Y. Takeda, T. Hirasa, *"Loss minimization of permanent magnet synchronous motor drives"*, IEEE Transactions on Industrial Electronics, v. 41, Oct. 1994, pp. 511-517.

[7] S. Bogosyan, M. Gokasan, *"Adaptive torque ripple minimization of permanent magnet synchronous motors for direct drive applications"*, IEEE Industry Applications Conference, v. 1, 1995, pp. 231-237.

[8] T. Batzel, K.Y. Lee, *"Commutation torque ripple minimization for permanent magnet synchronous motors with Hall effect position feedback"*, IEEE Transactions on Energy Conversion, v. 13, Sept. 1998, pp. 257-262.

[9] S. Clenet, Y. Lefevre, N. Sadowski, S. Astier, *"Compensation of permanent magnet motors torque ripple by means of current supply waveshapes control determined by a finite element method"*, IEEE Transactions on Magnetics, v. 29, March 1993, pp. 2019-2023.

[10] P.C. Kraus and O. Wasynzuk, *Electromechanical Motion Devices*, New York, McGraw-Hill, 1989

[11] E. Clarke, *Circuit Analysis of AC Power Systems, v. I, Symmetrical and related components*, John Wiley and sons, Inc. NY, NY, 1943

[12] V.R. Saksena, J. O'Reilly, and P.V. Kokotivic, *"Singular Perturbation and Time-scale methods in control theory: Survey 1976-1983"*, Automatica, v. 20, pp. 273-293, May 1984

[13] W.L. Brogan, *Modern Control Theory*, Prentice-Hall, Englewood Cliffs, NJ, 1991

[14] R. Sepe, J. Lang. *"Inverter non-linearities and discrete time vector current control"* IEEE Transactions on Industry Applications Vol. 30, no. 1 Jan 1994, pp. 62-70

[15] Weschta, A. Weverkirch, W. *"Nonlinear behavior of voltage source inverters with power transistors"* Proceedings of European conference on Power Electronics and applications (EPE), 1989 pp.533-577

[16] P. Vranka, G. Griva, F. Profumo, *"Practical improvement of a simple VI flux estimator for sensorless FO controllers operating in the low-speed region"* 24th Annual IECON Proceedings, 1998 v. 3 , 1998 , pp. 1615 -1620

[17] J. Holtz, *"Pulsewidth modulation – a survey"*, IEEE Transactions on Industrial Electronics, v. 39, no. 5, Dec. 1992, pp. 410-420.

[18] R.B. Sepe, H.L. Jeffrey, *"Implementation of discrete time field oriented current control"*, IEEE Transactions on Industry Applications, v.30, no. 3, June 1994, pp. 723-728

[19] D. Chung, S. Sul, *"Analysis and compensation of current measurement error in vector controlled ac motor drives"*, IEEE Transactions on Industry Applications, v. 34, no. 2, March, 1998, pp 340-345.

[20] D.M. Brod, D.W. Novotny, *"Current control of VSI-PWM inverters,"* IEEE ransactions on Industrial Applications, vol. IA-21, no. 4, pp. 562-570, 1985

[21] T.M. Rowan, R.J. Kerkman, *"A new synchronous current regulator and an analysis of current-regulated PWM inverters,"* IEEE Transactions on Industrial Applications, vol. IA-22, no. 4, pp. 678-690,1986.

[22] G. Champenois, P. Mollard, J. Rognon, *"Two digital torque control structures for inverter fed permanent magnet sinusoidal synchronous machines,"* IEEE Industrial Electronics, Control, and Instrumentation Conference, IECON Proceedings, pp. 725-730, 1988.

[23] T. Sebastian, *"Temperature effects on torque production and efficiency of PM motors using NdFeB magnets"*, IEEE Industry Applications Meeting, 1993, v. 1, pp.78-83.

[24] T.D. Batzel , K.Y. Lee, *"Rotor position estimation for a slotless permanent magnet synchronous motor with Hall sensor feedback"*, Naval Symposium on Electric Machines Proceedings, Oct. 1998, pp. 87-94